



Provided by the author(s) and University College Dublin Library in accordance with publisher policies. Please cite the published version when available.

Title	A review of the processing, composition and temperature-dependent mechanical and thermal properties of dielectric technical ceramics
Authors(s)	de Faoite, Daithí; Browne, David J.; Chang-Díaz, Franklin R.; Stanton, Kenneth T.
Publication date	2012-05
Publication information	Materials Science, 47 (10): 4211-4235
Publisher	Springer
Item record/more information	http://hdl.handle.net/10197/8477
Publisher's statement	The final publication is available at Springer via http://dx.doi.org/10.1007/s10853-011-6140-1 .
Publisher's version (DOI)	10.1007/s10853-011-6140-1

Downloaded 2022-08-23T04:30:35Z

The UCD community has made this article openly available. Please share how this access benefits you. Your story matters! (@ucd_oa)



A Review of the Processing, Composition, & Temperature-Dependent Mechanical and Thermal Properties of Dielectric Technical Ceramics

**Daithí de Faoite · David J. Browne ·
Franklin R. Chang-Díaz · Kenneth T. Stanton**

Received: date / Accepted: date

Abstract The current review uses the material requirements of a new space propulsion device, the Variable Specific Impulse Magnetoplasma Rocket (VASIMR[®]) as a basis for presenting the temperature dependent properties of a range of dielectric ceramics, but data presented could be used in the engineering design of any ceramic component with complementary material requirements. A material is required for the gas containment tube (GCT) of VASIMR[®] to allow it to operate at higher power levels. The GCT's operating conditions place severe constraints on the choice of material. A dielectric is required with a high thermal conductivity, low dielectric loss factor, and high thermal shock resistance. There is a lack of a representative set of temperature-dependent material property data for materials considered for this application and these are required for accurate thermo-structural modelling. This modelling would facilitate the selection of an optimum material for this component. The goal of this paper is to determine the best material property data values for use in the materials selection and design of such components. A review of both experimentally and theoretically-determined temperature-dependent & room temperature properties of several materials has been undertaken. Data extracted are presented by property. Properties reviewed are density, Young's, bulk and shear moduli, Poisson's ratio, tensile, flexural

Daithí de Faoite
School of Electronic, Electrical and Mechanical Engineering, University College Dublin, Belfield, Dublin 4, Ireland

David J. Browne
School of Electronic, Electrical and Mechanical Engineering, University College Dublin, Belfield, Dublin 4, Ireland

Franklin R. Chang-Díaz
Ad Astra Rocket Company, 141 W. Bay Area Blvd., Webster, Houston, TX 77598, U.S.A.

Kenneth T. Stanton*
School of Electronic, Electrical and Mechanical Engineering, University College Dublin, Belfield, Dublin 4, Ireland

*Corresponding Author:

Tel.: +353-1-716-1918

Fax: +353-1-283-0534

E-mail: Kenneth.Stanton@ucd.ie

and compressive strength, thermal conductivity, specific heat capacity, thermal expansion coefficient and the factors affecting maximum service temperature. Materials reviewed are alumina, aluminium nitride, beryllia, fused quartz, sialon and silicon nitride.

Keywords electric propulsion · plasma · space materials · gas containment tube · thermal properties · mechanical properties · ceramics

1 Introduction

The Variable Specific-Impulse Magnetoplasma Rocket [1] (VASIMR[®]) is an advanced electric propulsion rocket pioneered at the NASA Advanced Space Propulsion Laboratory, and currently being developed by the Ad Astra Rocket Company, Houston, Texas. It uses strong, shaped magnetic fields to contain and direct a high-power plasma for high-specific impulse propulsive thrust. The plasma is created using helicon electromagnetic waves [2] in what is thereby known as the helicon section of the engine. A gas containment tube (GCT) is used in this helicon section to contain the neutral gas prior to ionisation and to ensure physical separation between the neutral gas and the helicon antenna. The helicon plasma generation process is not completely efficient and results in large amounts of the input RF-energy being lost as waste heat. This heat is deposited on the inner surface of the GCT by the processes of volumetric radiation, Bohm diffusion, and collisions from high-temperature neutral atoms [3]. Excessive temperatures in the helicon section from this waste heat may pose a problem, not only to the structural integrity of the gas containment tube, but also to the operation of the superconducting magnets required to contain the plasma [4].

The heat flux from the plasma is not only large but is also non-uniformly distributed over the inside surface of the GCT, and a material used for this application must be capable of dissipating this waste heat to a heat exchanger or radiator. Peak heat loads have been observed downstream of and directly under the helicon antenna [5]. The non-uniformity of the heat deposition leads to high localised temperatures and large temperature gradients in the GCT walls. Furthermore, during operation, the RF power may be cycled on and off repeatedly, inducing cyclic thermal stresses in the components of the engine.

The conditions under which the material must operate place stringent constraints on the materials that can be used. A fully dense material is required with high strength, high thermal conductivity, and high thermal shock resistance. Good dielectric properties are also required in order to minimise dielectric heating from the helicon antenna. The selection of materials for this application has many similarities to the constraints imposed in the selection of materials for microwave and RF waveguide windows, radomes for missiles and supersonic aircraft, dielectric components in ion engines and hall thrusters, and dielectric heat spreaders in electronics.

Fused quartz has been used successfully as the GCT material in previous VASIMR[®] prototype engines [2, 6]. Fused quartz has also been used in other large diameter helicon plasma sources [7], and widely used as a gas containment tube material in helicon plasma sources for plasma-assisted coating and sputtering applications [8], (where commonly referred to as a ‘discharge tube’). Pyrex[®] has also been used as a GCT material in low power helicon plasma sources [9, 10]. Borosilicate glass has been used as the material in a small-diameter plasma discharge tube [11]. Alumina and sapphire have also been used as plasma containment tube materials [12–15]. However, the current 200 kW VASIMR[®] prototype poses a significantly greater challenge than that faced by most plasma generation sources, due to the large physical size and very large heat fluxes. This prototype rocket will have

approximately twice the total electrical power input of the previous prototype in order to increase the amount of thrust generated by the rocket. Selection of a suitable material for the GCT of the prototype is thus required. The candidate materials considered in this analysis are alumina (Al_2O_3), aluminium nitride (AlN), beryllia (BeO), sialon, and silicon nitride (Si_3N_4).

When selecting a material for such an application, or when modelling or optimising such a component, the designer requires dependable representative material property data. During the detailed design process it is best to conduct a series of standardised tests on the chosen material, or selection of materials, from different manufacturers in order to verify their properties. However, it is usually impractical at the outset of the design process to test a vast number of different material types from different vendors. The focus of this paper is to find a set of representative, self-consistent values of material properties for several high performance commercially available ceramics being considered for use for the VASIMR[®] GCT, which may be used for such modelling and preliminary selection.

Values of thermophysical properties are widely taken as constants with respect to temperature in design, despite the clear variation in some properties with temperature. For hardware components which must dissipate large amounts of waste heat, such as the VASIMR[®], temperature-dependent material property data are critical for component design, simulation, and materials selection, and to allow accurate prediction of the effects of thermal shock and fatigue, and the component's susceptibility to thermal stress induced failure. Variations in ceramic material properties with temperature are typically detrimental from a design point of view; with increases in temperature causing decreases in strength, moduli, thermal conductivity, electrical resistivity, and increases in thermal expansion coefficient and dielectric loss factor. Room temperature material property values are useful for identifying a number of different materials that could be feasibly used, but failure to use temperature-dependent data in simulations can lead to inadequate designs, due to the simultaneous deterioration of many properties.

The focus of this analysis is on literature-derived data for commercially available material grades. It is not intended to be an exhaustive review of all existing data, but instead a representative summary of typical temperature dependent data. Property data, where available are widely scattered, especially in the cases of fused quartz and sialon. Temperature-dependent data are not available for every material property for each material, but have been presented where possible. Comparatively limited data are available for Weibull analyses [16] of ceramic strengths in the literature, especially at elevated temperatures. Hence, strength data are presented only in terms of mean values. Representative thermal and mechanical property data for alumina, aluminium nitride, beryllia, sialon and silicon nitride are presented, along with data for fused quartz. The material properties considered are listed in Table 1. Points plotted in each graph represent data-points from the original reports; dashed lines are a guide to the reader's eye. Solid lines represent data presented in the form of curves rather than discrete data-points in the original reports. Details regarding measurement techniques may be found in the original reports.

Several of the properties considered are intrinsic to the inter-atomic bonding in the material, namely density, elastic moduli, Poisson's ratio, specific heat capacity and thermal expansion coefficient. Extrinsic "properties" are strongly dependent upon external factors such as processing, forming, finishing and environmental conditions. Flexural, tensile and compressive strength, and thermal conductivity are considered extrinsic material properties due to their dependence on external factors. However, although the intrinsic material properties are directly related to inter-atomic bonding, the property exhibited by the bulk polycrystalline material is to a greater or lesser extent still affected by processing. For ex-

ample, sintering temperature affects bulk density, which in turn affects the elastic moduli. Sintering conditions can also affect the amount of inter-granular glass formed, thus affecting the thermal expansion coefficient. Intrinsic material properties are only independent of processing in single crystals.

Table 1 Material properties considered.

Mechanical	Thermal
Density	Thermal Conductivity
Young's Modulus	Specific Heat Capacity
Bulk Modulus	Thermal Expansion Coefficient
Shear Modulus	
Poisson's Ratio	
Tensile Strength	
Flexural Strength	
Compressive Strength	

2 Ceramic Materials for the GCT

Ceramic material properties are strongly dependent on raw powder, impurity, and sintering aid composition, and on forming and sintering parameters. For tractability, this study focuses on one particular material specification for each candidate material, based on one or more of: material purity, relative density, sintering aids, and mean grain size. The specification in each case is chosen to be representative of a high performance commercially available material, in an attempt to bound the performance envelope of each material class. Material property data have been compiled from published original experimental studies, and from some first principle computational physics studies. Data compiled in some previous material property reviews are also considered. An excellent review of the mechanical and thermal properties of α -alumina is provided by Munro [17] up to elevated temperatures. Alumina is considered in this review for completeness: some data values from the Munro review [17] are given, along with data from more recent studies, and different studies of alumina not included in the Munro review. Where known, manufacturer-supplied data are not used. Every attempt has been made to find data corresponding to these specifications, and where data are unavailable, data for similar material specifications are used, and the differences in composition is noted. Material specifications are summarised in Table 2.

2.1 Alumina

α -Alumina (Al_2O_3), the industry standard for electronic substrates [18], is widely used in high heat flux electrical insulation, electronic packaging, and structural applications due to its relatively high strength, thermal conductivity, maximum service temperature, good chemical inertness, excellent dielectric properties and low cost relative to other technical ceramics. Alumina is also widely used as a cutting tool, and RF window material, and is a candidate material for various applications in ITER [19–21]. ITER, a tokamak fusion

plasma device, similarly requires dielectric materials with high thermal diffusivity and low loss tangent in many areas.

Alumina is available in a wide range of purities, with thermal and mechanical properties improving with increasing purity and relative density. 0.2 wt% MgO is commonly used as a sintering aid for Al_2O_3 to prevent anomalous grain growth. The material specification for alumina is sintered α - Al_2O_3 with purity ≥ 99.5 wt%, relative density of $\geq 98\%$ and a nominal grain size of $5 \mu\text{m}$ [17], consistent with typical high performance, high purity commercial grades of alumina.

2.2 Aluminium Nitride

Aluminium nitride (AlN) has very high RT thermal conductivity for a ceramic, second only to beryllia, with an intrinsic thermal conductivity of $319 \text{ W m}^{-1} \text{ K}^{-1}$ along the c -axis at 300 K [22], high-purity single crystal RT thermal conductivity of $285 \text{ W m}^{-1} \text{ K}^{-1}$ along the c -axis [22], and sintered body RT thermal conductivities over $265 \text{ W m}^{-1} \text{ K}^{-1}$ reported [23, 24], although careful control of material composition and processing conditions is required to produce high thermal conductivity bodies [25]. The thermal shock resistance of aluminium nitride is even higher than that of beryllia due to its lower coefficient of thermal expansion, closely matched to that of silicon. AlN is an attractive, non-toxic alternative to BeO for high power electronic substrates, packages and heat spreaders, where thermal management is a significant design issue [26–34]. Other applications of AlN include its use for boats and crucibles for the production of high purity GaAs for semiconductor applications [35], and AlN has also been considered for use as a ballistic armor material [36]. However, use of AlN in structural applications has been limited, despite its good room temperature and elevated temperature mechanical properties. This is primarily due to high cost, typically making use of AlN only feasible where heat flux issues are severe. AlN has good oxidation resistance, due to the formation of a passivating alumina coating, even as high as 1400°C [37].

The thermal conductivity of AlN ceramics is greatly affected by the presence of metallic impurities [38], and oxygen impurity [39–41] present on the surface of the starting AlN powder in the form of Al_2O_3 due to spontaneous reaction with air, and also dissolved in the AlN lattice. The lattice distortion due to aluminium vacancies resulting from incorporation of oxygen into the lattice leads to increased phonon scattering, thus lowering the thermal conductivity of the material [25, 42–46].

Rare-earth or alkaline-earth oxide additives are commonly used to facilitate liquid-phase sintering by reaction of the additive with Al_2O_3 on the surface of the AlN powder, forming liquid phases [25] which promote densification. The additives are also used to react with oxygen impurity diffused from the AlN grains to the grain boundaries, forming secondary phase aluminates, thus reducing the number of oxygen defects and enhancing the thermal conductivity [25]. Yttria is the most commonly used sintering aid for AlN [47]. Achievement of maximum thermal conductivity requires optimisation of the amount of additive, balancing between purification of AlN grains and formation of low thermal conductivity aluminate secondary phases [25].

Segregation of secondary phases from AlN grains occurs during annealing. Long annealing times or very high annealing temperatures facilitate the migration of aluminate secondary phases to the surface of the sintered body, with subsequent evaporation from the surface, improving the thermal conductivity [25]. However, annealing leads to grain growth

which, although contributing to enhancement of thermal conductivity, can reduce strength. AlN without additives typically requires hot pressing to achieve densification.

Fully dense AlN can be achieved by pressureless sintering with sintering aids. Structural AlN components are produced by either hot pressing or sintering. A typical high performance commercially available grade of AlN is sintered, starting from a powder of 98.9 wt% Al+N and 1.1 wt% oxygen impurity content, to which 4.9 wt% Y_2O_3 —an amount equimolar to the oxygen in the form of Al_2O_3 present in the AlN powder—is added. A nominal grain size of 7 μm and a relative density of $\geq 99\%$ is specified.

2.3 Beryllia

The room temperature thermal conductivity of beryllia (BeO) is the highest of any ceramic, close to that of high conductivity metals, but decreases rapidly between room temperature and 200°C. Its high thermal conductivity gives beryllia excellent thermal shock resistance, despite a high thermal expansion coefficient, and only moderate strength. BeO is extremely expensive, resulting from high powder cost and safety precautions required during powder handling and processing due to the fact that it is toxic. Despite its toxicity, the combination of excellent thermal and dielectric properties, including low relative permittivity and dielectric loss tangent, make beryllia a candidate material for a diverse range of high-technology applications. BeO is used in high-power and high-frequency electronic applications for electronic substrates, heat sinks, and insulators where high heat dissipation is required [18], in X-ray windows and high-power laser tubes, and in high-power RF-waveguide windows [48]. BeO is also considered for use in military applications for radomes and missile nosecones [49]; in aerospace applications for rocket motor nozzles; in materials processing applications as a refractory for molten metal handling and as a crucible and crucible-liner material; in nuclear applications for reactor moderator rods and neutron reflectors [50]; and as a potential material for vacuum windows of coaxial transmission lines in ITER [19, 51].

Typical impurities present in BeO powders include Fe, Mg, Ca and Al [52,53]. SO_3 and SO_4 impurities may also be present in sulphate-derived powders, such as Brush-Wellman (now Materion Ceramics, 6100 South Tucson Blvd., Tucson, AZ 85706, U.S.A.) grade UOX, remaining after the production of the BeO powder by decomposition of beryllium sulphate salt [52, 53]. BeO typically also has a number of significant anionic impurities, including F, P, S and Si, typically not stated by manufacturers in the total impurity content [54]. These anionic impurities contribute to the reduction in strength of BeO at moderate and high temperatures requiring the use of high purity powders, particularly powders low in F, P, S and Si to retain good strength at these temperatures [54]. However, these anionic impurities also assist in the densification of BeO through reaction with a MgO sintering aid [54]. MgO, in the presence of impurities, has been found to be an effective sintering aid to promote densification of BeO [52, 54], typically added in quantities of ≈ 0.5 wt%. Iron is one of the most significant impurities in BeO, increasing the sinterability of BeO, allowing sintering to be achieved faster and/or at lower temperatures. However, Fe impurity leads to flaws and inhomogeneities in the sintered ceramic, and may also limit the achievable maximum sintered density [55]. Significant Fe pickup can occur from steel powder mixing equipment, particularly during long mixing times [53], and green body compaction equipment, which can lead to large irregular grains on the surface of the sintered ceramic [55]. Similarly, carbon pickup can occur from dies and pressing equipment, particularly affecting the surface layer of the BeO ceramic [56]; this necessitates the use of machining to remove this layer [54].

Cold uniaxial pressing [53], isostatic pressing and extrusion [55] are the most common techniques commercially used for forming green bodies from BeO powder [57], with large BeO bodies typically formed by isopressing [57]. Extrusion leads to some preferential grain orientation, the *c*-axis tending to align with the extrusion axis [58,59], leading to some anisotropy in the sintered body [57]. BeO may be hot pressed [54], although this is less commercially prevalent than sintering. Hot pressing of BeO can achieve simultaneously higher density and finer grain size than sintering [54]. However, the shape of components that may be produced is typically somewhat limited to simple shapes; complex shapes require specially-designed dies [54]. Hot pressing of BeO typically results in an anisotropic microstructure, with preferential alignment of the elongated *c*-axis of acicular grains in a plane perpendicular to the hot pressing direction with random orientation within this plane [60,61].

The densification rate of BeO during sintering reduces above 94-95%td (6-5% porosity) due to isolation of grain boundary porosity, becoming very significant above 2.90 g cm^{-3} (96.4%td) [53, 55]. Subsequent reduction in porosity, via longer sintering times or higher temperatures, occurs slowly, and at the expense of increased grain growth [53, 55]. Peak strength in sintered BeO typically occurs in the density range $2.81\text{--}2.93\text{ g cm}^{-3}$, due to the conflicting effects of densification and grain growth [53].

A typical high performance grade of beryllia, is 99.5 wt% pure BeO. A typical commercially available grain size of $15\text{ }\mu\text{m}$, giving a good balance between strength and thermal conductivity, is specified here. Typical relative density for sintered beryllia is $\approx 94.8\%$ with very low porosity bodies only being attainable at the expense of increased grain growth or use of hot pressing [54]. High purity starting powders are required, as anionic impurities, especially Si, F, P and S lead to lower strength at moderate temperatures [54].

2.4 Fused Quartz

The near-zero thermal expansion coefficient of fused quartz over a wide temperature range results in excellent thermal shock resistance. This property, combined with adequate strength, excellent corrosion resistance, ablation resistance, and excellent electrical and dielectric properties, make fused quartz the material of choice for a wide range of applications, including radomes, radar windows, combat and space vehicles [62], vacuum windows [63, 64], boats and crucibles for high temperature material handling and fabrication, and high power lamp tubing. Due to the high purity of fused quartz, its properties are very sensitive to small changes in composition and thermal history [65]. The hydroxyl content of fused quartz is one of the major impurities that affects its properties.

The typical high-performance commercially available grade of fused quartz specified here has less than 50 ppm total elemental impurities by weight, corresponding to a nominal purity of $\geq 99.995\text{ wt}\%$ SiO_2 . Flame melting of the quartz crystals is specified as the processing route, but data for material produced by electrical melting of quartz crystals are considered where data are unavailable for material produced by a flame melting route. A fully dense amorphous material with no bubble inclusions is specified.

2.5 Sialon

Sialon (or 'SiAlON') is a solid solution based on silicon nitride, with Al^{3+} and O^{2-} replacing Si^{4+} and N^{3-} in the crystal lattice [66-70], resulting in a material with high strength, wear resistance, thermal shock resistance and oxidation resistance [71]. The phases of sialon

of interest for engineering applications are α' [72, 73] ($M_x\text{Si}_{12-(m+n)}\text{Al}_{m+n}\text{O}_n\text{N}_{16-n}$, ($x \leq 2$), where M is a metal cation), isostructural with α - Si_3N_4 , and β' [66, 67] ($\text{Si}_{6-z}\text{Al}_z\text{O}_z\text{N}_{8-z}$, ($0 \leq z \leq 4.2$)), isostructural with β - Si_3N_4 , with duophase $\alpha' + \beta'$ sialons also in common use. β' -sialon is the most widely used sialon, with higher fracture toughness ($\approx 7\text{--}8 \text{ MPa}\cdot\text{m}^{\frac{1}{2}}$ for β' -sialon, $\approx 3\text{--}4 \text{ MPa}\cdot\text{m}^{\frac{1}{2}}$ for α' -sialon [74]) and room temperature strength, but lower hardness ($\approx 1500\text{--}1700 \text{ kg}\cdot\text{mm}^{-2} \text{ H}_v$ for β' -sialon, $\approx 1900\text{--}2100 \text{ kg}\cdot\text{mm}^{-2} \text{ H}_v$ for α' -sialon) and thermal shock resistance than α' -sialon [71, 75, 76]. A good combination of strength, hardness, and fracture toughness, intermediate to those of monolithic α' and β' -sialons, can be obtained from duplex sialons [75], with hardness and thermal shock resistance increasing and toughness decreasing with increasing α' -phase content [71, 77]. The higher lattice asymmetry and increased defects from greater Al-O and Si-N substitution, and presence of interstitial cations, results in lower thermal conductivity in α' -sialon due to increased phonon scattering [78].

Oxynitride glasses occur as grain boundary phases (intergranular film at triple point junctions) in Si_3N_4 and sialon ceramics, due to reaction of alumina and metal oxide sintering aids (such as yttria and other rare-earth oxides) with SiO_2 on the surface of the Si_3N_4 powder forming a liquid, which aids densification via liquid phase sintering [79]. The thermo-mechanical properties of oxynitride glasses depend on various factors, including N:O ratio, modifier cations present and relative amounts of these modifier cations [79]. The properties of the oxynitride glass and the volume fraction present control the bulk properties of the sialon (or silicon nitride), having lower elastic moduli and higher thermal expansion coefficients than the sialon (or silicon nitride) grains [79]. The oxynitride glassy grain boundary phase typically present in β' -sialon ceramics leads to a deterioration in chemical and mechanical properties at elevated temperatures [71], reducing high temperature strength and creep resistance due to glassy phase softening. This limits the practical maximum operating temperature to approximately 1000°C . Increasing the nitrogen content incorporated into the oxynitride glass results in higher glass transition temperature, viscosity, hardness, elastic moduli, and a decrease in the thermal expansion coefficient due to increased cross-linking in the glass due to presence of N atoms [79].

For oxynitride glasses containing rare-earth cations, a decrease in the cation radius results in higher glass transition temperature, viscosity and Young's modulus [79]. Lower viscosity oxynitride glass formed during sintering allows easier densification, but impairs creep resistance: metal cations such as Dy, Lu, Er and Ho have smaller ionic radii than Y, and thus form higher viscosity oxynitride glasses with improved creep resistance [79].

The cations of metal oxide sintering aids used to stabilise the α' -phase in the production of α' -sialon may be interstitially incorporated into the solid solution, and this results in reduced volume of intergranular glassy phase [71]. α' -sialons consequentially retain their mechanical properties better at elevated temperatures and have a higher maximum operating temperature (up to 1400°C).

Sialons may be heat-treated, and this partially or fully crystallises the oxynitride grain boundary glass, forming a glass-ceramic or fully crystalline ceramic leading to improvement in elevated temperature properties [79]. Complete devitrification is capable of raising the maximum operating temperature from $\approx 1000^\circ\text{C}$ to $\approx 1400^\circ\text{C}$. The crystalline phases formed depend on the original glass composition and heat treatment parameters, and typically have considerably better mechanical properties than the parent glass (e.g. $E > 200 \text{ GPa}$) [79].

β' -sialon typically has acicular grains [71, 80], while α' -sialon typically has equiaxed grain structure [71], but can be produced with a bimodal equiaxed-acicular microstructure by

careful selection of starting composition and control of sintering conditions, or use of elongated seed crystals in the starting powder [81], with resultant improved fracture toughness and thermal shock resistance [82]. The intrinsically higher fracture toughness of β' -sialon is due to the *in situ* reinforced microstructure. The equiaxed microstructure typically found in single phase α' -sialon leads to lower room temperature flexural strength, typically in the range 350–500 MPa (compared to \approx 700–1100 MPa for β' -sialon), with higher reported values for single phase α' -sialons with acicular grains or duophase sialons with high α' -phase content.

α' -phase sialon can transform to β' -phase at high temperature in the presence of liquid phase oxynitride glass [71, 79]. The stability of the α' -phase is dependent upon the metal cations present in the sintering aid, and the ability to stabilise the α' -phase is a major consideration in the selection of a sintering aid for α' -sialon. Sintering aids used for α' -sialon are typically Y [76], Ca, Mg, Li, or rare-earth metals (such as Nd, Sm [75], Dy, Yb [83]) except La and Ce [71], with dysprosium (Dy) found to be very effective at stabilising the α' -phase [75, 84]. There have been a number of studies on suppressing α' - β' phase transformation, with subsequent improvement in material properties.

The most common formation route for α' -sialon is by direct sintering of α - Si_3N_4 , AlN, Al_2O_3 and other metal oxide powders [71]. Liquid-phase sintering is achieved by reaction of Al_2O_3 and metal oxide sintering aids with SiO_2 on the surface of the Si_3N_4 powder, forming a liquid phase which aids densification [79]. Sialon may also be fabricated by nitridation of powders and post-sintering [71], typically with higher resultant porosity and inferior mechanical properties than direct sintering. A large number of studies have been conducted on the preparation of sialon ceramics over the past four decades [85], with significant improvement in sialon properties achieved. The retention of many desirable properties at elevated temperatures, including strength, wear resistance, hardness, corrosion and oxidation resistance, creep resistance, good thermal shock resistance and low coefficient of thermal expansion, makes sialons promising materials for a wide range of high temperature, high stress applications in corrosive environments. Applications of sialons include cutting tools, dies, diesel fuel valves and weld locator pins [86]. Sialons are also considered as candidate materials for, amongst other applications, radomes [87] and gun barrel liners [83].

α' -sialons have many superior properties to β' -sialons salient to the application being addressed here, including higher thermal shock resistance and higher maximum service temperature, despite their lower thermal conductivity and strength at room temperature and intermediate temperatures. However, research into α' -sialons is still less mature than for β' -sialons, and the vast majority of commercially available sialons are β' -phase or duophase. In addition, the data on the mechanical properties of α' -sialons are widely scattered, partly due to microstructural and compositional variation [71]. Therefore, for this review, β' -sialon is selected as the nominal phase, but data for duophase sialons are also considered. Y- β' -sialon with 6 wt% Y_2O_3 sintering aid is chosen as the material specification for this work, with relative density of $\geq 99.0\%$, nominal grain size of 2 μm , and nominal purity of 94 wt% $\text{Si}_3\text{N}_4 + \text{AlN} + \text{Al}_2\text{O}_3$. Given the volume of ongoing research into α' -sialons, and their attractive intrinsic properties, it is conceivable that α' -sialons will surpass β' -sialons as a candidate material for this application in the coming years.

2.6 Silicon Nitride

Silicon nitride (Si_3N_4) is one of the most attractive materials for high temperature structural and electronic applications, due to its hot strength, toughness, thermal shock resistance,

thermal conductivity, and dielectric properties. It has two polymorphic forms of interest; α and β [88, 89]. α -phase Si_3N_4 —a metastable phase under ordinary pressures [90] with lower thermal conductivity—transforms to β - Si_3N_4 at high temperature, making β - Si_3N_4 more suitable for engineering applications [91]. Silicon nitride for structural applications may be produced near theoretical density by a variety of processing methods, including hot pressing (HPSN), hot isostatic pressing (HIPSN), pressureless sintering (SSN), gas pressure sintering (GPSSN) and sinter-reaction bonding (SRBSN), with material properties dependent upon processing route. The 15–30% porosity typical in reaction-bonded silicon nitride (RBSN) results in comparatively inferior mechanical ($\sigma_f \approx 200$ MPa [92], $E \approx 130$ –200 GPa) and thermal properties [93], making it less suitable for structural applications. SRBSN is produced by nitriding a mixture of silicon powder and sintering aids, green-machining, and then sintering to densify the component. An advantage of the SRB process is that it allows near-net shape fabrication of complex Si_3N_4 components, whereas HP and HIP processes only allow for the production of simply shaped components, with any post-sinter grinding adding significantly to component cost. HIP results in the highest strength silicon nitrides, comparable to that of HPSN (800–1200 MPa), with that of SSN slightly lower (600–1000 MPa) [92]. SRBSN has shown the greatest potential for having simultaneously high thermal conductivity and strength [94]. The toughening effect of silicon nitride's bimodal microstructure, due to crack bridging, is controlled by the size and volume fraction of the large acicular grains [81]. Extensive research over the past four decades has significantly improved the thermal [91], creep [95, 96], and mechanical properties of silicon nitrides [81], notably simultaneously improving strength, fracture toughness [81] and thermal conductivity [94]. Strong, high thermal conductivity Si_3N_4 ceramics may be attainable with use of high-purity sub-micron powders, and careful selection of sintering aids.

Due to the low diffusion coefficient of silicon nitride [71], densification requires the use of sintering aids to facilitate liquid phase sintering by formation of an oxynitride glass [79]. Pressureless sintering of silicon nitride requires large additions of sintering aids to achieve full densification [76]. Some of the oxynitride glassy phase always remains, impacting on the material's mechanical properties, particularly at high temperatures [71], limiting the maximum operating temperature to ≈ 1000 –1200°C [92]. Fully dense HIPSN and HPSN can be produced with very small additions of sintering aids, yielding reduced glassy phase. This results in excellent mechanical properties which are retained to higher temperatures, with maximum operating temperatures of ≈ 1200 –1300°C [76, 92]. Typical sintering aids used for the densification of silicon nitride are yttria (Y_2O_3), alumina (Al_2O_3), magnesia (MgO), and rare-earth oxides, either singly or in combination [71, 91], with calcium oxide (CaO) and various other compounds also successfully used. Al_2O_3 is an inexpensive sintering aid, but unlike Y_2O_3 and MgO it forms a solid solution in the Si_3N_4 grains, leading to significantly lower thermal conductivity. Use of MgO and Y_2O_3 sintering aids in combination yields low porosity, high strength silicon nitride [97].

The combination of thermal, dielectric, wear, and superior high-temperature mechanical properties has led to implementation of silicon nitride in a wide range of ambient and high-temperature structural and electronic applications, including cutting tools, turbocharger rotors, reciprocating engine valves, bearings, rocket motor components, electronic substrates and heat sinks, RF waveguides, windows and radomes. Silicon nitride has been long proposed for use in the hot section of gas turbines, as rotors, stators and combustion liners, but deployment has been limited due to low fracture toughness, which limits impact resistance, and oxidation and environmental degradation in the high-temperature, high-velocity combustion environment which leads to removal of the SiO_2 protective layer [81].

SRBSN is selected as the nominal production route for Si_3N_4 for the current work, due to its potential for having simultaneously high thermal conductivity and strength [94]. Data are also considered for SSN, HPSN and HPSN materials representative of commercially available silicon nitrides. A typical high-performance commercially available grade of silicon nitride is sinter reaction bonded β - Si_3N_4 produced with 5 wt% MgO, 4 wt% Y_2O_3 sintering aids, corresponding to 91 wt% purity of silicon nitride powder mix. The expected microstructure is bimodal with fine $\approx 2 \mu\text{m}$ equiaxed grains and larger acicular grains with average major axis length $\approx 10 \mu\text{m}$. A relative density of $\geq 99\%$ is specified.

Table 2 Summary of material properties considered.

	Alumina	Aluminium Nitride	Beryllia	Fused Quartz	Sialon	Silicon Nitride
Processing	Sintered	Sintered	Cold Pressed & Sintered	Flame Melted	Sintered	Sinter Reaction Bonded
Additives	≤ 0.5 wt% MgO	4.9 wt% Y_2O_3	≤ 0.5 wt% MgO	None	6 wt% Y_2O_3	5 wt% Y_2O_3 + 4 wt% MgO
Phase	α	α	α	Amorphous	β'	β
Purity	≥ 99.5 wt%	94.0 wt%	99.5 wt%	99.995 wt%	94 wt%	92 wt%
Relative Density	$\geq 98\%$	$\geq 99\%$	94.8%	100%	$\geq 99\%$	$\geq 99\%$
Nominal Grain Size	$5 \mu\text{m}$	$7 \mu\text{m}$ Polyhedral	$15 \mu\text{m}$ Equiaxed	Amorphous	$2 \mu\text{m}$	$2 \mu\text{m}$ Equiaxed & $10 \mu\text{m}$ Acicular

3 Structural Material Properties

3.1 Density

The practical bulk density of the six materials in this study, as supplied commercially, is sought. Density is dependent upon the amounts and types of sintering aids used; such as the high molecular mass sintering aids commonly used with AlN, sialon and Si_3N_4 such as Y_2O_3 ; upon the presence of other impurities, and upon the resulting secondary phases formed [76].

The theoretical density of pure ceramic crystals may be calculated from measurements of the lattice parameters. For hexagonal lattices the unit cell has volume $V = (\sqrt{3}/2) a^2 c$, where a and c are the respective lattice parameters. The theoretical density can be calculated from:

$$\rho_{\text{th}} = \frac{Mz}{N_{\text{A}}V} \quad (1)$$

where z is the number of formula units per unit cell, N_{A} is Avogadro's number and V is the unit cell volume, and M is the molar mass. The theoretical density may be used as an estimate of the bulk density of very low porosity polycrystalline ceramics in the absence of significant secondary phases or intra-granular solid solution formation. For sintered AlN, sialon and Si_3N_4 the large mass fraction of sintering aids typically used precludes the use of this calculation method for accurate estimation of sintered ceramic density. Direct experimental measurements of ceramic density at high temperature are typically not found in the literature, but elevated temperature measurements of lattice parameters from X-ray

diffraction and linear thermal expansion from dilatometry may be used to assess variations in density with temperature.

Taylor & Lenie [37] calculated the theoretical density of AlN to be $\approx 3.26 \text{ g}\cdot\text{cm}^{-3}$ from lattice parameter measurements of single crystals. Hot pressing of AlN to very low levels of porosity with little or no sintering aid addition results in a practical bulk density very close to this theoretical value (e.g. as measured in [98]). However, low-porosity sintered or hot pressed AlN with additions of high molecular mass sintering aids such as Y_2O_3 have bulk densities higher than this, with bulk density typically increasing with increasing sintering aid addition [28]. By analysing the data, the density of fully dense AlN may be approximated by:

$$\rho_{\text{Y-AlN}} \cong 3.26 + 13 \times 10^{-3} \xi_{\text{Y}_2\text{O}_3} \quad (2)$$

where $\xi_{\text{Y}_2\text{O}_3}$ is the yttria addition in wt%.

Commercial BeO is typically produced with density $\approx 2.85 \text{ g}\cdot\text{cm}^{-3}$, having $\rho_{\text{th}} \approx 94.7\%$, or to a lesser extent with density $\approx 2.90 \text{ g}\cdot\text{cm}^{-3}$ and $\rho_{\text{th}} \approx 96.3\%$. Beryllia may be produced near full density, but typically at the expense of increased grain growth, with corresponding deterioration in mechanical properties. A theoretical density of $3.008 \text{ g}\cdot\text{cm}^{-3}$ was calculated for BeO by Lillie [58] from lattice parameter measurements, and is used by several authors (e.g. by Beaver *et al.* [52]). However, a more extensive analysis of lattice parameter values from the literature indicates that the true theoretical density is $\approx 3.0104 \text{ g}\cdot\text{cm}^{-3}$, with a value of $3.010 \text{ g}\cdot\text{cm}^{-3}$ being widely used in the literature (e.g. in [54]).

The density of fused quartz is significantly lower than that of the ceramics considered in this study. Sosman [99] notes relatively large variations in literature values of density of vitreous silica, both within specimens and between different specimens, on the order of 0.1%—much more scatter than for literature values of crystalline quartz—possibly due to composition, type of silica from which the vitreous silica was made, temperature history during manufacture, strain fields in the glass, or small amounts of impurities.

The density of the α' -sialon, β' -sialon, and oxynitride glassy phases are approximately $3.28 \text{ g}\cdot\text{cm}^{-3}$, $3.18 \text{ g}\cdot\text{cm}^{-3}$ and $4.00 \text{ g}\cdot\text{cm}^{-3}$ respectively [76]. The density of the β - Si_3N_4 phase is approximately $3.2 \text{ g}\cdot\text{cm}^{-3}$. The lattice volume of α - Si_3N_4 is 0.55% larger than that of β - Si_3N_4 per Si_3N_4 unit [90].

Experimental measurements of density are plotted in Figure 1.

3.2 Young's, Bulk & Shear Moduli

The elastic moduli, including the Young's, shear and bulk moduli, and the Poisson's ratio, of isotropic solid materials may be calculated from measurements of the density and longitudinal and shear sound velocities by ultrasonic methods [17, 102, 111]:

$$E = \rho \left(\frac{3V_L^2 V_S^2 - 4V_S^4}{V_L^2 - V_S^2} \right) \quad (3)$$

$$G = \rho V_S^2 \quad (4)$$

$$K = \rho \left(V_L^2 - \frac{4}{3} V_S^2 \right) \quad (5)$$

$$\nu = \frac{V_L^2 - 2V_S^2}{2(V_L^2 - V_S^2)} \quad (6)$$

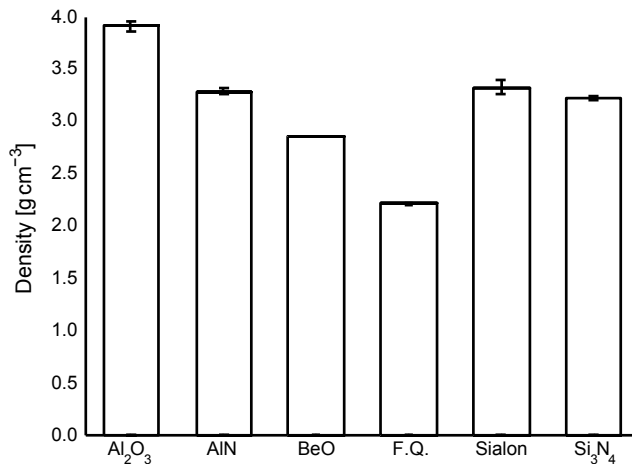


Fig. 1 RT Density values averaged from the following references: Al₂O₃-1, CoorsTek AD995 alumina [100]; Al₂O₃-2, Coors AD-998 alumina [101]; Al₂O₃-3, Wesgo AL-998 Alumina [101]; Al₂O₃-4, review of alumina [17]; AlN-1, Cercom hot pressed AlN [98]; AlN-2, HP AlN with ≈ 4 wt% Y₂O₃ [102]; AlN-3, sintered AlN with 0.5 mol% Y₂O₃ [103]; AlN-4, sintered AlN 5 wt% Y₂O₃ [28]; AlN-5, sintered AlN 4.91 wt% Y₂O₃ [25]; AlN-6, Cerac HP AlN [104]; AlN-7, HP AlN [105]; BeO-1, Brush-Wellman 995 BeO [101]; F.Q.-1, review of fused quartz [99]; F.Q.-2, Toshiba Ceramics T-1030 fused quartz [106]; F.Q.-3, PECVD fused quartz film [107]; F.Q.-4, KU1 fused quartz [108]; F.Q.-5, Heraeus Infracel 301 fused quartz [108]; Sialon-1, Kennametal TK4 sialon [100]; Sialon-2, sintered sialon 6 wt% Y₂O₃ [76]; Sialon-3, Kennametal TK4 sialon [83]; Si₃N₄-1, Ceradyne Ceralloy 147-31N silicon nitride [100]; Si₃N₄-2, Kyocera SN235P silicon nitride [100]; Si₃N₄-3, SR3 silicon nitride [94]; Si₃N₄-4, SR6 silicon nitride [94]; Si₃N₄-5, sintered Si₃N₄ with 1 mol% Y₂O₃ and 1 mol% Nd₂O₃ [109]; Si₃N₄-6, sintered Si₃N₄ with 2 mol% Al₂O₃ and 2 mol% Y₂O₃ [109]; Si₃N₄-7, HP Si₃N₄ with 3.5 wt% Y₂O₃ [110]; Si₃N₄-8, HP & HIP Si₃N₄ with 3.5 wt% Y₂O₃ [110].

where E , G and K are the Young's, shear and bulk moduli respectively, ν is the Poisson's ratio, V_L and V_S are the longitudinal and shear sound velocities respectively, and ρ is the density. In addition to ultrasonic methods, elastic moduli may be determined by a variety of experimental methods, including calculation of E from flexural tests and calculation of K from isostatic compressive tests. The first-order elastic response of isotropic solid materials is fully constrained by any two such moduli. The remaining two constants may be calculated by the standard relations:

$$E = 2G(1 + \nu) \quad (7)$$

$$K = \frac{E}{3(1 - 2\nu)} \quad (8)$$

$$\nu = \frac{3K - E}{6K} \quad (9)$$

$$G = \frac{3KE}{9K - E} \quad (10)$$

In order to ensure consistency between recommended values, curve fit equations for all elastic properties are solved simultaneously, constrained by these relations. A further consistency measure is to recognise that the Poisson's ratio must always be in the range $0 < \nu < 0.5$ [112], and will be ≈ 0.2 – 0.3 for almost all of the materials under investigation, while for fused quartz $\nu \approx 0.17$. Differences between measurement of adiabatic and isothermal elastic values are ignored, the adiabatic moduli being assumed. Above 1000°C, plasticity

effects greatly influence the apparent elastic moduli calculated from static measurements such as flexural tests, so dynamic methods are preferred [58].

The Young's, shear and bulk moduli are strongly dependent upon the porosity of a ceramic, decreasing sharply initially, and then more gradually with increasing porosity. The porosity dependence of elastic moduli can be estimated by a simple linear model at very low porosities, while over a broad range of porosities the relationship is non-linear. A great number of models have been proposed to describe the variation in elastic moduli with porosity [113–116], notably including those of Hasselman [117] and Knudsen [118]. However, variation of elastic moduli is dependent not only on the volume of porosity but also its morphology, precluding use of one model to describe the variation for all materials [119].

The elastic properties of most non-cubic ceramic crystals are anisotropic, but polycrystalline ceramics composed of randomly oriented grains typically exhibit approximate macroscopically isotropic behaviour [17]. However, processing routes which lead to preferential grain orientations, such as hot pressing, can result in macroscopic anisotropic behaviour [104, 120]. De With and Hattu [104] measured differences in the Young's modulus of hot pressed AlN without sintering aids in directions parallel and perpendicular to the hot pressing direction, while Fryxell & Chandler [59] observed anisotropic elastic moduli in BeO with preferential grain orientation, extruded and sintered from BeO powder containing needle-like crystals.

Crystals of the hexagonal crystal system have only 5 independent elastic constants: C_{11} , C_{12} , C_{13} , C_{33} and C_{44} [121], the elastic constant C_{66} being given by $C_{66} = \frac{1}{2}(C_{11} - C_{12})$. Consistency criteria apply, limiting the valid range of elastic constant values, based on lattice stability [122, 123]. The compliance matrix may be evaluated from single-crystal ultrasonic wave velocity measurements or by other means. The macroscopically pseudo-isotropic elastic moduli of a fully-dense ceramic composed of randomly oriented crystals may be estimated from the single-crystal elastic moduli using the Voigt-Reuss-Hill (VRH) approximation [124–126]. The isotropic VRH estimation of the bulk modulus is:

$$K_{\text{VRH}} = \frac{C_{11} + 2C_{12}}{3} \quad (11)$$

while the VRH estimation of the shear modulus is the average of the Voigt and Reuss limits on shear modulus:

$$G_{\text{VRH}} = \frac{G_{\text{V}} + G_{\text{R}}}{2} \quad (12)$$

$$G_{\text{V}} = \frac{(C_{11} - C_{12}) + 3C_{44}}{5} \quad (13)$$

$$G_{\text{R}} = \frac{5C_{44}(C_{11} - C_{12})}{(4C_{44} + 3(C_{11} - C_{12}))} \quad (14)$$

where C_{ij} are the relevant coefficients of the compliance matrix, and G_{V} and G_{R} are the Voigt and Reuss limits on shear modulus respectively. From these relations the VRH approximation of the Young's modulus and Poisson's ratio may be calculated using the standard relations for isotropic solid materials. Chung and Buessem [127] assert that the VRH method provides a good approximation to the polycrystalline elastic moduli for materials with single-crystal elastic anisotropy of < 10%, defined by:

$$A^* = \left(\frac{3(A-1)^2}{3(A-1)^2 + 25A} \right) \times 100 \quad [\%] \quad (15)$$

where:

$$A = \frac{2C_{44}}{C_{11} - C_{12}} \quad (16)$$

Reviews of elastic moduli of ceramics inevitably must consider data from materials of slightly different porosity levels. Correlation of data of different porosities, including calculations of moduli for the theoretically dense material using the VRH approximation, into porosity models allows for the estimation of the moduli at the nominally specified porosity level.

The presence of secondary phases affects the elastic moduli of ceramics (porosity being a limiting case of a secondary phase of zero stiffness). Glassy grain boundary phases are present in many ceramics, as discussed in Sections 2.5 and 2.6, of varying volume fraction and morphology, leading to large differences in measured moduli values for ostensibly similar compositions. Oxynitride glassy phases found in sialons and silicon nitrides have lower elastic moduli ($\approx 120\text{--}170$ GPa) than the primary phase, reducing the Young's, shear and bulk moduli of the bulk material [79].

The derivative with respect to temperature of any elastic constant tends towards zero approaching absolute zero [128], while a linear dependence of Young's modulus with respect to temperature has been observed for many crystalline solids at high temperatures [128]. A simple linear fit has been used by several researchers for the temperature dependence of elastic moduli, as the deviation from linear variation with temperature is small except at low temperatures [129]. However, this fit can lead to a slight over-estimation of the room temperature Young's modulus from intermediate or high temperature data. The Wachtman equation has been shown to accurately describe the temperature dependence of Young's modulus—provided the variation in Poisson's ratio with temperature is small—or bulk modulus, across a broad range of temperature for various non-metallic crystals and polycrystalline ceramics [128, 130]:

$$Y = Y_0 - B \cdot T \cdot \exp\left(\frac{-T_0}{T}\right) \quad (17)$$

where Y_0 is the Young's or bulk modulus at 0 K, and both T_0 [K] and B [GPa.K⁻¹] are empirical fitting parameters, related to the Debye temperature and Grüneisen parameter. The slope of the Wachtman equation tends to $-B$ at high temperature. The parameter T_0 is relatively sensitive to small variations or errors in Young's or bulk moduli data [102]. Some deviation from linear behaviour of Young's modulus of alumina has been observed by Wachtman & Lam [131] and Fukuhara & Yamauchi [132] at very high temperatures, and this is attributed to grain boundary slip [131]. Wolfenden [133] and Sánchez-González *et al.* [134] observed that the rate of decrease of Young's modulus with temperature of two commercially supplied aluminas increases rapidly above 600–800°C, possibly due to grain boundary sliding arising from softening of a glassy secondary phase [134]. The rate of decrease of Young's modulus with temperature in the studies of Wolfenden and Sánchez-González *et al.* is significantly greater than that seen in many other studies of alumina, possibly due to larger volume fraction of glassy grain boundary phase, or occurrence of a brittle-to-ductile transition.

In contrast to polycrystalline ceramics, the elastic moduli of fused quartz increase with increasing temperature.

Data for Young's, bulk and shear moduli of all materials are plotted in Figures 2, 3 and 4 respectively.

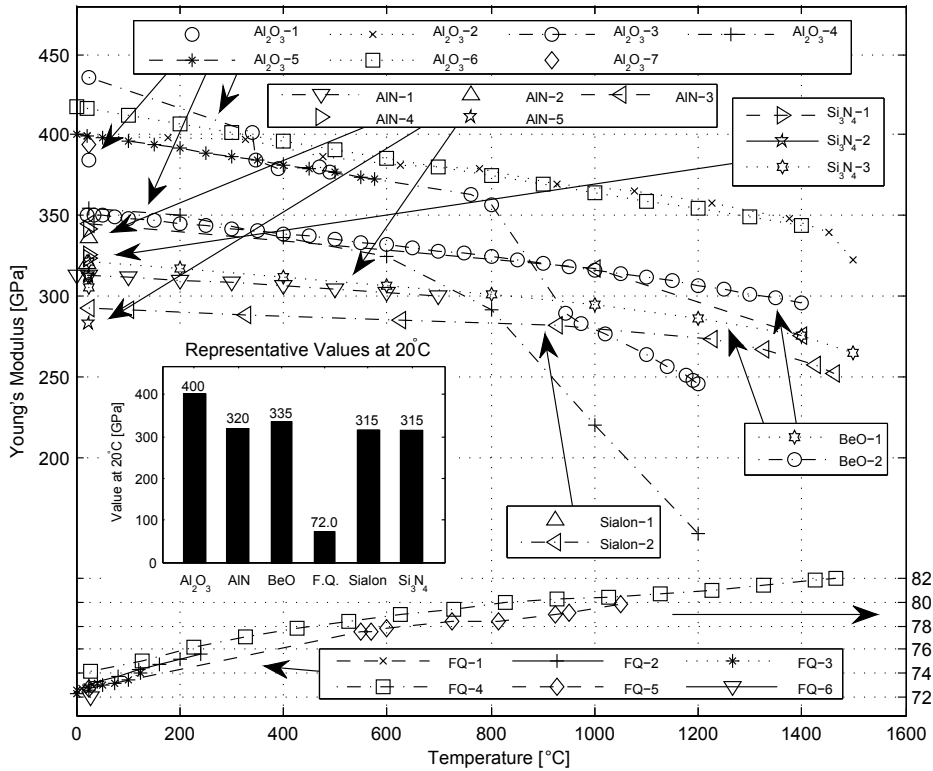


Fig. 2 Young's modulus values from the following references: Al₂O₃-1, CoorsTek AD995 alumina [100]; Al₂O₃-2, near-theoretical density alumina [132]; Al₂O₃-3, McDanel Refractory Company 99.8% pure alumina [133]; Al₂O₃-4, Goodfellow 98% dense alumina [134]; Al₂O₃-5, sintered alumina [128]; Al₂O₃-6, review of alumina [17]; Al₂O₃-7, hot pressed & HIPped alumina [135]; AlN-1, HP AlN with ≈ 4 wt% Y₂O₃ [102]; AlN-2, Cercom HP AlN [98]; AlN-3, HP AlN [37]; AlN-4, Cerac HP AlN [104]; AlN-5, Keramont Corporation sintered AlN [136]; BeO-1, beryllia [58]; BeO-2, 94.8%t.d. BeO [59]; F.Q.-1, clear fused silica [137]; F.Q.-2, optical quality fused silica [138]; F.Q.-3, Toshiba Ceramics T-1030 fused quartz [106]; F.Q.-4, Toshiba Ceramics T-1030 fused quartz [139]; F.Q.-5, fused silica [140]; F.Q.-6, PECVD fused quartz film [107]; Sialon-1, Kennametal TK4 sialon [100]; Sialon-2, near-theoretical density β -sialon [132]; Si₃N₄-1, Ceradyne Ceralloy 147-31N silicon nitride [100]; Si₃N₄-2, Kyocera SN235P silicon nitride [100]; Si₃N₄-3, GTE Laboratories PY6 HIP silicon nitride [141].

3.3 Poisson's Ratio

The Poisson's ratio, ν , of polycrystalline ceramics is relatively insensitive to temperature compared to other elastic parameters, being widely taken as a constant, although some variation with temperature does occur [132]; typically it increases with temperature for the materials considered in this review. Poisson's ratio can be calculated from ultrasonic measurements or static (e.g. flexural) measurements. At high homologous temperatures the effects of creep become increasingly more pronounced causing static measurements of Poisson's ratio to approach a limiting value of 0.5 [58], and this makes dynamic measurement more suitable. Poisson's ratio may also be calculated from the Young's and shear moduli:

$$\nu = \left(\frac{E}{2G} - 1 \right) \quad (18)$$

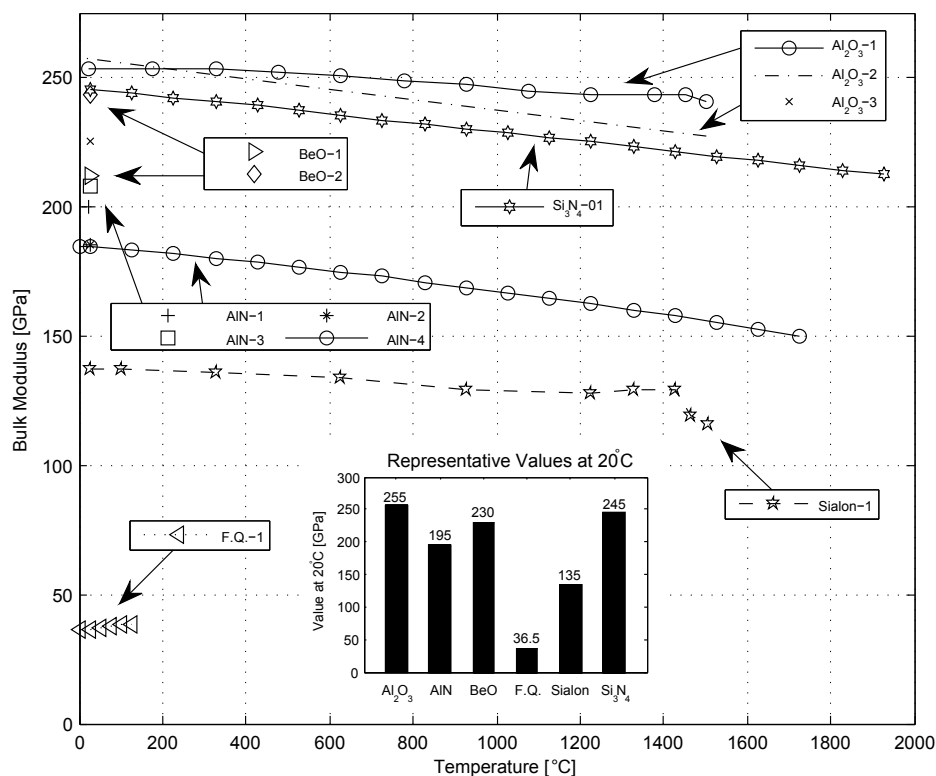


Fig. 3 Bulk modulus values from the following references: Al₂O₃-1, near-theoretical density alumina [132]; Al₂O₃-2, review of alumina [17]; Al₂O₃-3, hot pressed & HIPped alumina [135]; AlN-1, Cercom HP AlN [98]; AlN-2, 99.99% pure AlN [142]; AlN-3, Tokuyama Soda & Toshiba Ceramics AlN [143]; AlN-4, theoretical calculation for AlN [144]; BeO-1, single crystal BeO [145]; BeO-2, 99.88%t.d. polycrystalline BeO [146]; F.Q.-1, Toshiba Ceramics T-1030 fused quartz [106]; Sialon-1, near-theoretical density β -sialon [132]; Si₃N₄-1, theoretical calculation for β -Si₃N₄ [90].

This relation holds only for isotropic materials, but may be applied to polycrystalline materials composed of randomly oriented anisotropic grains [147]. However, large variations are present in Poisson's ratio measurements reported in the literature for the ceramic materials considered in this study. This may partly result from calculating the Poisson's ratio from Young's and shear moduli, which are calculated in turn from sound velocities or resonance frequencies, with small errors in Young's and shear moduli leading to large errors in Poisson's ratio.

Experimental data are plotted in Figure 5.

3.4 Flexural Strength

There is a very wide variation in values reported for flexural strength of materials in the literature, due in part to differences in testing environment and surface finish [150]. In addition, flexural strength measurements must be treated cautiously, as the measured value depends upon the test configuration (3 or 4-point bend) and sample dimensions. For a given specimen size, the stressed volume in a three-point bend test is smaller, resulting in higher

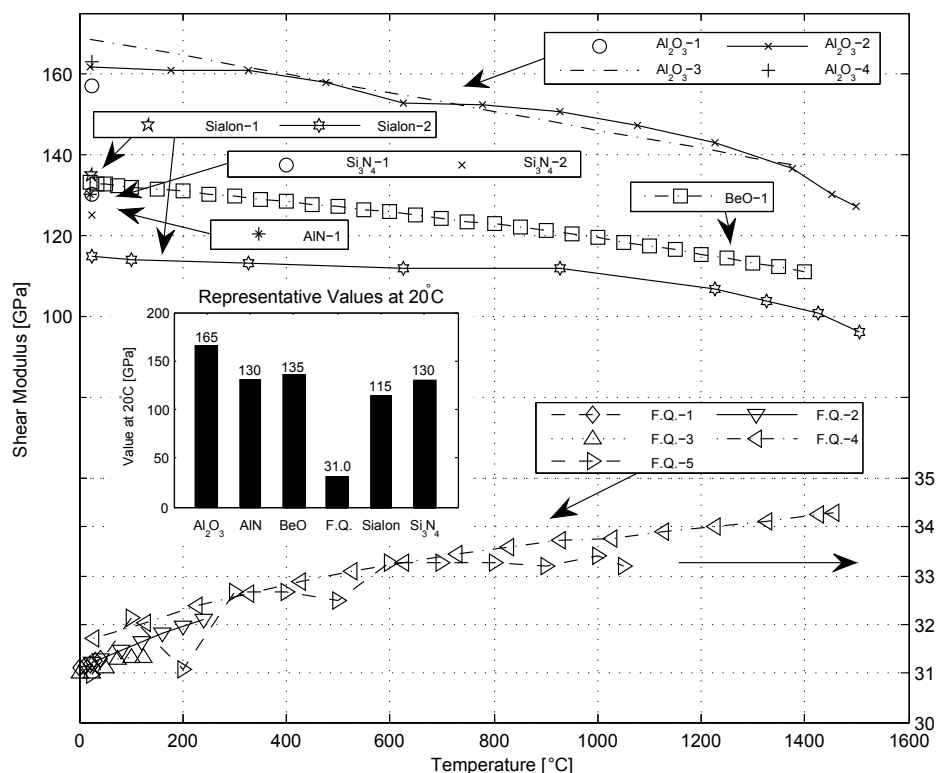


Fig. 4 Shear modulus values from the following references: Al_2O_3 -1, CoorsTek AD995 alumina [100]; Al_2O_3 -2, near-theoretical density alumina [132]; Al_2O_3 -3, review of alumina [17]; Al_2O_3 -4, hot pressed & HIPped alumina [135]; AlN-1, Cercom HP AlN [98]; BeO-1, 94.8%t.d. BeO [59]; F.Q.-1, clear fused silica [137]; F.Q.-2, optical quality fused silica [138]; F.Q.-3, Toshiba Ceramics T-1030 fused quartz [106]; F.Q.-4, Toshiba Ceramics T-1030 fused quartz [139]; F.Q.-5, fused silica [140]; Sialon-1, Kennametal TK4 sialon [100]; Sialon-2, near-theoretical density β -sialon [132]; Si_3N_4 -1, Ceradyne Ceralloy 147-31N silicon nitride [100]; Si_3N_4 -2, Kyocera SN235P silicon nitride [100].

measured values of strength. The measured strength of ceramics is also dependent upon the strain rate of the measurement. Data presented here are for strain rates typical of quasi-static flexural, tensile or compressive tests (loading rate $\approx 0.5 \text{ mm}\cdot\text{min}^{-1}$), intermediate to those of shock testing and creep testing. At high homologous temperatures, creep in ceramics becomes a significant design issue, requiring careful creep analysis, but collation of creep data is beyond the scope of this paper.

Sintered or hot pressed alumina is commercially available in a wide range of purities, with strength increasing with increasing purity. Some very high flexural, tensile and compressive strength values have been reported in the literature for carefully prepared aluminas, produced from high-purity powders, with low porosity, small grain size, and lacking the glassy grain boundary phases typically present in commercially supplied alumina [135, 151–153]. These materials are not representative of commercially available alumina, and so are not included here. At room temperature, elimination of H_2O from the test environment, such as by testing in vacuum, leads to a significant increase in the flexural strength of alumina by eliminating slow crack growth [150]. Reported values of flexural strength of sintered AlN are very sparse in the literature, but quite a large number of RT flexural strength data are

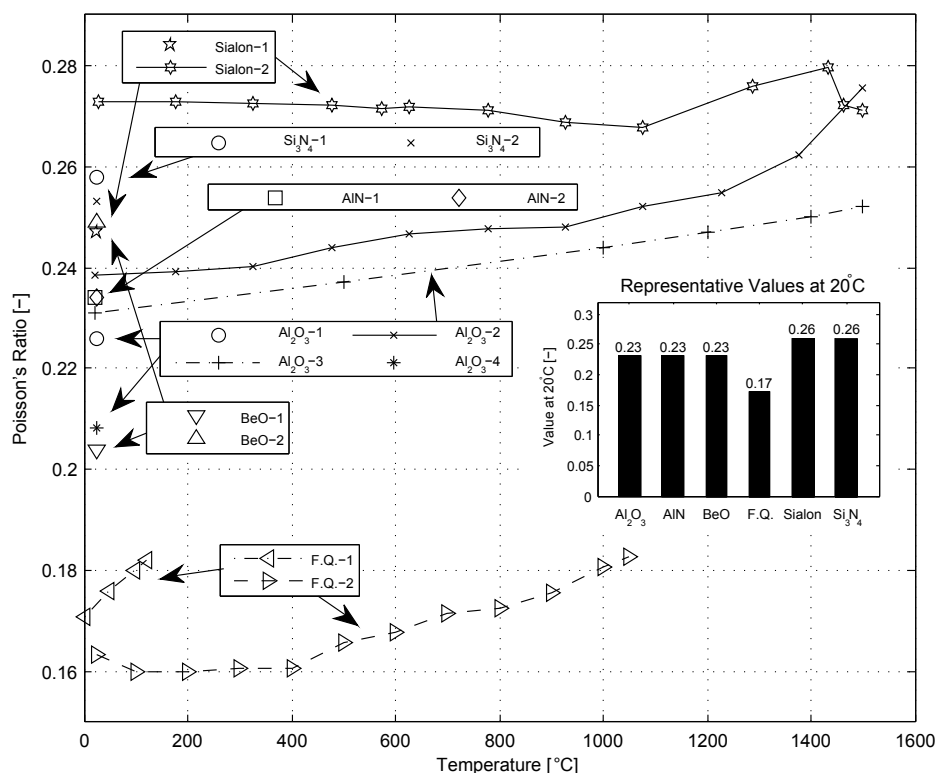


Fig. 5 Poisson's ratio values from the following references: Al₂O₃-1 CoorsTek AD995 alumina [100]; Al₂O₃-2, near-theoretical density alumina [132]; Al₂O₃-3, review of alumina [17]; Al₂O₃-4, hot pressed & HIPped alumina [135]; AlN-1, Cercom HP AlN [98]; AlN-2, Dow Chemical Corporation HP AlN [148]; BeO-1, fully dense BeO [58]; BeO-2, single crystal BeO [149]; F.Q.-1, Toshiba Ceramics T-1030 fused quartz [106]; F.Q.-2, fused silica [140]; Sialon-1, Kennametal TK4 sialon [100]; Sialon-2, near-theoretical density β -sialon [132]; Si₃N₄-1, Ceradyne Ceralloy 147-31N silicon nitride [100]; Si₃N₄-2, Kyocera SN235P silicon nitride [100].

available for hot pressed AlN, and these are presented in Figure 6, along with the data for the other materials reviewed.

High temperature flexural strength data for AlN are very scarce. AlN typically has an RT strength intermediate to that of alumina and beryllia. Some relatively high values, above 390 MPa, for RT flexural strength of AlN have been reported, mostly for polished specimens [154, 155], or electronic substrates [26, 27]. De With and Hattu [104] measured a dependence of flexural strength of hot pressed AlN on surface roughness, with flexural strength decreasing significantly for a greater surface roughness for a hot pressed AlN, from 310 MPa for surface finish $R_a = 0.2 \mu\text{m}$, decreasing to 237 MPa for $R_a = 1.1 \mu\text{m}$. Other studies reporting the variation of RT flexural strength with surface condition for AlN are also reviewed by De With and Hattu [104]. However, the high strength values reported for polished specimens are not representative of commercially available structural AlN bodies. Y₂O₃ has been found to be an effective additive for producing high density, high strength sintered AlN, while Sm₂O₃ or La₂O₃ have been shown to result in still higher strengths, in excess of 400 MPa [156].

Reported experimental values for the flexural strength of BeO at room temperature and elevated temperatures are scarce [57]. The strength of BeO typically increases above room temperature, reaching a strength maximum between 500–1200°C, and then decreases rapidly at higher temperatures [54, 57, 59, 150]. However, the maxima are not always observed. Porosity, or high additive or impurity contents, which can dominate the failure mode, can reduce or eliminate the strength maxima, giving a strength plateau at intermediate temperatures [150]. Fryxell and Chandler [59] reported the increase in strength from room temperature to the strength maximum at intermediate temperature to be larger, and occur at higher temperature, with increasing grain size. Carniglia *et al.* [54] ascribed the strength minima observed around room temperature in their three-point flexural strength tests of hot pressed BeO to chemisorbed moisture. Some authors have reported the strength of BeO measured in vacuum to be higher than when measured in air [157]. For a given porosity level the RT flexural strength of BeO increases with decreasing grain size. However, attainment of very high densification in BeO is only attainable by either hot pressing or by sintering at high temperatures, or for long isothermal hold times, resulting in large grain sizes and thus a reduction in strength. Clare [53] found that fine grain sizes in low porosity sintered BeO could only be attained with powders with low Fe impurity. Hot pressing of BeO typically results in higher densification for a given final grain size than pressureless sintering, and this results in higher strength. For pressureless sintering, an optimal compromise between densification and grain size is typically found in the grain size range 5–20 μm , with relative density $\geq 95\%$ [49, 59]. Even still, the typical flexural strength of BeO is lower than that of the other ceramics considered in this study, with some RT values as low as 100–150 MPa reported [49, 52]. Typical RT values given by suppliers of commercially available sintered BeO are given in the range 175–275 MPa, although these values are unsubstantiated in the formal literature. Flaws limiting the strength of sintered BeO include areas of high porosity and fine grain size, areas of coarse grain size resulting from high Fe content, areas of coarse grain size resulting from segregated impurities of Al, Mg and Si, and very large elongated grains up to 200 μm in length [53].

β' -sialon typically has a bimodal equiaxed-acicular microstructure with interlocking grains leading to high RT flexural strength, increasing with more pronounced acicular grain structure [85]. The typical RT flexural strength of duplex α'/β' -sialons is also high, due to the presence of elongated β' -grains. The RT strength of many single-phase α' -sialons, which typically have an equiaxed grain structure, is significantly less than those of β' -sialons (≈ 400 MPa [158]). The flexural strength of α' -sialons may be improved by promoting the formation of elongated grains, by careful selection of starting composition and control of sintering conditions, or use of elongated seed crystals in the starting powder [81, 159, 160]. Glassy oxynitride grain boundary phases in sialon result from reaction of sintering aids for liquid phase sintering to promote densification, and the oxide layer on silicon nitride powders [78]. Softening of the grain boundary phase at elevated temperatures leads to a reduction in strength. Reduced grain boundary phase in α' -sialons leads to retention of flexural strength up to higher temperatures [71].

The flexural strength and fracture toughness of silicon nitride is higher than most other monolithic ceramics, due in part to the presence of interlocking elongated β - Si_3N_4 grains, resulting in an *in situ* reinforced microstructure [81]. This self-reinforced microstructure, consisting of small, mainly equiaxed grains, and large elongated interlocking grains—analogue to whisker or fibre-reinforced ceramic composites [81]—leads to cracks propagating through the intergranular films, preventing intragranular fracture, leading to crack bridging by the elongated grains [81]. Sintering aids added to facilitate liquid-phase sintering may react with oxygen in the Si_3N_4 powder and form glassy intergranular films,

which significantly affect the material's strength, both at room temperature and elevated temperatures. The composition of the intergranular films are mainly determined by the sintering aids added. The intergranular glass affects the densification of silicon nitride and growth of the elongated β - Si_3N_4 grains during sintering. The flexural strength of Si_3N_4 typically decreases in a gradual monotonic fashion with increasing temperature up to ≈ 800 – 1200°C , although some strength increases with temperature have been reported, especially in RBSN [150]. Experimental studies reporting high temperature strength of silicon nitride typically do not report strength at intermediate temperatures, so interpolation from room temperature strengths over a large temperature difference must often be used. At higher temperatures, the strength of silicon nitride falls off more rapidly. The hot strength of Si_3N_4 and sialon is dependent upon the grain boundary phase, which softens at elevated temperatures leading to a decrease in strength. The properties of the grain boundary phase, including the volume fraction, crystallinity, composition, and subsequent viscosity and glass transition temperature—all primarily determined by sintering aid addition—control the hot strength of Si_3N_4 . Silicon nitride hot pressed with minimal sintering aids results in a very small volume fraction of grain boundary phase, leading to higher RT strength and retention of strength up to higher temperatures than for sintered silicon nitride. Use of MgO and Y_2O_3 sintering aids in combination has been found to result in good densification and high flexural strength [97].

3.5 Tensile Strength

Tensile strength measurements of structural ceramics, particularly at elevated temperatures are very sparse in the literature. Tensile strength measurements of ceramics typically provide greater accuracy than flexure tests, but are often disfavoured due to prohibitively higher costs [136]. Tensile (σ_t) and flexural (σ_f) strengths can be related using Weibull scaling [164], where details of the dimensions of the flexural and tensile test specimens, but not the flaw size, are required [105]:

$$\sigma_f = \sigma_t \left(\frac{v_t}{v_f} \right)^{\frac{1}{m}} \quad (19)$$

where v_t and v_f are the effective volume of the tensile and flexural specimens respectively, and m is the Weibull modulus of the tensile specimens. In the flexural test, the effective stressed volume is smaller, so the flaw population which could initiate failure is smaller. Toutanji *et al.* [105] note that a conventional set of bend tests of 10–30 specimens could thus miss critical flaw populations such as agglomerates, which a tensile test—interrogating a much larger stressed volume—would not miss. Thus, calculating flexural strengths from tensile strength data by Weibull scaling yields conservative values for flexural strength; but calculating tensile strengths from flexural strength data leads to an over-estimation of tensile strength [99, 105].

Data for σ_t of all materials are plotted in Figure 7.

Having considered flexural and tensile strength, it is interesting to note that very little data are available for compressive strength of the materials considered in this study, particularly at elevated temperatures. Data obtained are plotted in Figure 8.

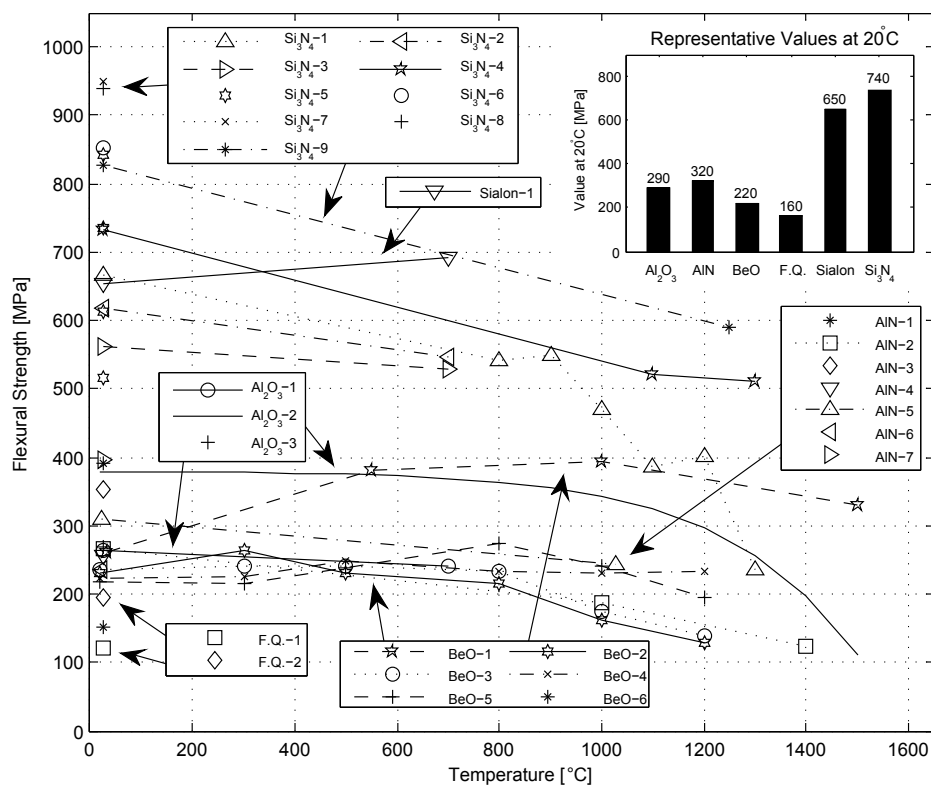


Fig. 6 Flexural strength values from the following references: Al₂O₃-1, CoorsTek AD995 alumina [100]; Al₂O₃-2, review of alumina [17]; Al₂O₃-3, Wesgo AL995 alumina [161]; AlN-1, tape-cast, dry pressed & sintered AlN [27]; AlN-2, HP AlN [37]; AlN-3, sintered AlN with 5 wt% Y₂O₃ [156]; AlN-4, Keramont Corporation sintered AlN [136]; AlN-5, Cerac Hot Pressed AlN with $R_a \approx 0.2 \mu\text{m}$ [104]; AlN-6, Cerac Hot Pressed AlN with $R_a \approx 1.1 \mu\text{m}$ [104]; AlN-7, HP AlN [105]; BeO-1, high purity hot pressed BeO with 100%t.d. and 20 μm grain size [54]; BeO-2, BeO from AOX powder, 2.90 g·cm⁻³, 10 μm grain size [59]; BeO-3, BeO From AOX Powder, 2.90 g·cm⁻³, 20 μm grain size [59]; BeO-4, BeO from UOX powder, 2.90 g·cm⁻³, 10 μm grain size [59]; BeO-5, BeO from UOX powder, 2.90 g·cm⁻³, 20 μm grain size [59]; BeO-6, sintered BeO from UOX Powder, 2.86 g·cm⁻³, grain size 28 μm [52]; F.Q.-1, KS-4V fused quartz [108]; F.Q.-2, KS-4V fused quartz [108]; Sialon-1, Kennametal TK4 sialon [100]; Si₃N₄-1, sintered silicon nitride [162]; Si₃N₄-2, Ceradyne Ceralloy 147-31N silicon nitride [100]; Si₃N₄-3, Kyocera SN235P silicon nitride [100]; Si₃N₄-4, GTE Laboratories PY6 HIP silicon nitride [141]; Si₃N₄-5, sinter-reaction-bonded silicon nitride [94]; Si₃N₄-6, 98%t.d. pressureless sintered Si₃N₄ with 5 wt% MgO and 3 wt% Y₂O₃ [97]; Si₃N₄-7, 99%t.d. pressureless sintered Si₃N₄ with 5 wt% MgO and 4 wt% Y₂O₃ [97]; Si₃N₄-8, 98%t.d. pressureless sintered Si₃N₄ with 5 wt% MgO and 5 wt% Y₂O₃ [97]; Si₃N₄-9, AlliedSignal GN-10 HIP Si₃N₄ [163].

4 Thermal Material Properties

4.1 Specific Heat Capacity

Specific heat capacity, considered here at constant pressure (c_p), is not strongly sensitive to microstructural or compositional differences. For multi-phase compounds, c_p may be accurately estimated from mass fraction weighted averaging of c_p of the constituent phases. The effect of large additions of sintering aids on c_p may thus be quantified. Beryllia, composed

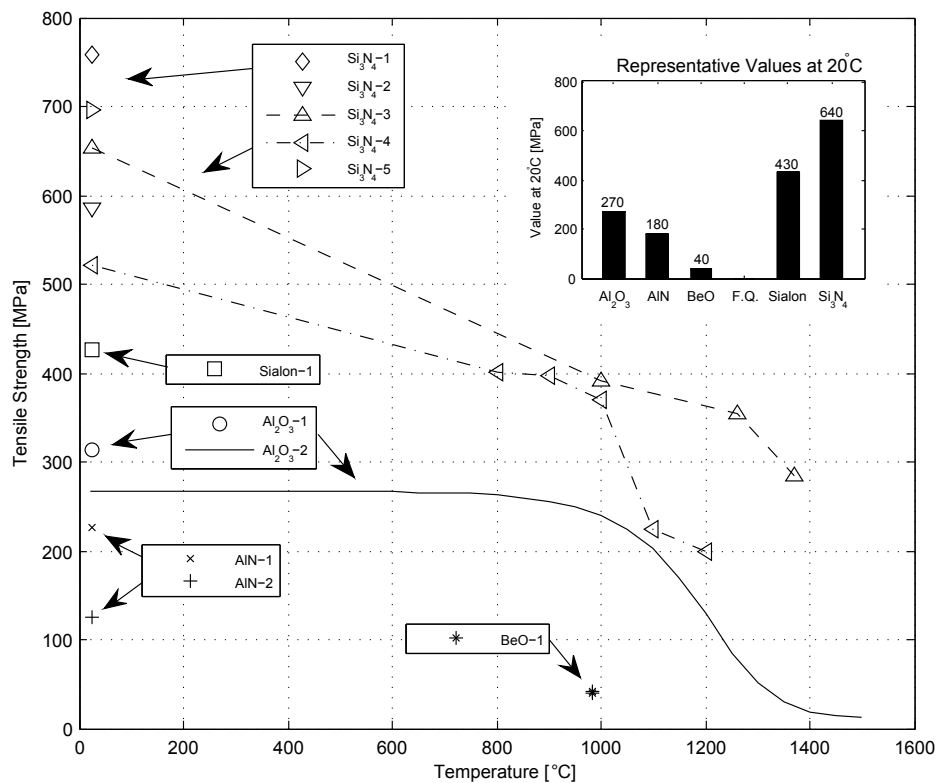


Fig. 7 Tensile strength values from the following references: Al₂O₃-1, CoorsTek AD995 alumina [100]; Al₂O₃-2, review of alumina [17]; AlN-1, HP AlN [105]; AlN-2, Keramont sintered AlN [136]; BeO-1, HP BeO [165]; Sialon-1, Kennametal TK4 sialon [100]; Si₃N₄-1, Ceradyne Cerallloy 147-31N silicon nitride [100]; Si₃N₄-2, Kyocera SN235P silicon nitride [100]; Si₃N₄-3, GTE Laboratories PY6 HIP silicon nitride [141]; Si₃N₄-4, sintered silicon nitride [162]; Si₃N₄-5, Allied Signal GN-10 silicon nitride [166].

of low atomic mass atoms, has a much higher specific heat capacity than the other ceramics considered in this study. For fused quartz, the data provided by Kelley [168] are taken as the recommended curve up to 2000 K, interpolated back to 0°C, being in excellent agreement with the data of Sosman [99] in this temperature range [169].

Data for c_p of all materials are plotted in Figure 9.

4.2 Thermal Conductivity

The thermal conductivity of a crystalline electrically insulating solid may be calculated from [176, 177]:

$$\lambda = \frac{1}{3} \bar{\rho} \bar{c}_V t_{ph} v_{ph} \quad (20)$$

where $\bar{\rho}$ is the molar density [kg.mol⁻¹], \bar{c}_V is the molar specific heat capacity at constant volume [J.mol⁻¹.K⁻¹], t_{ph} is the phonon mean free path [m], and v_{ph} is the mean phonon velocity [m.s⁻¹], which is approximately independent of temperature. The phonon mean free path is affected by intrinsic phonon-phonon scattering, which is temperature dependant,

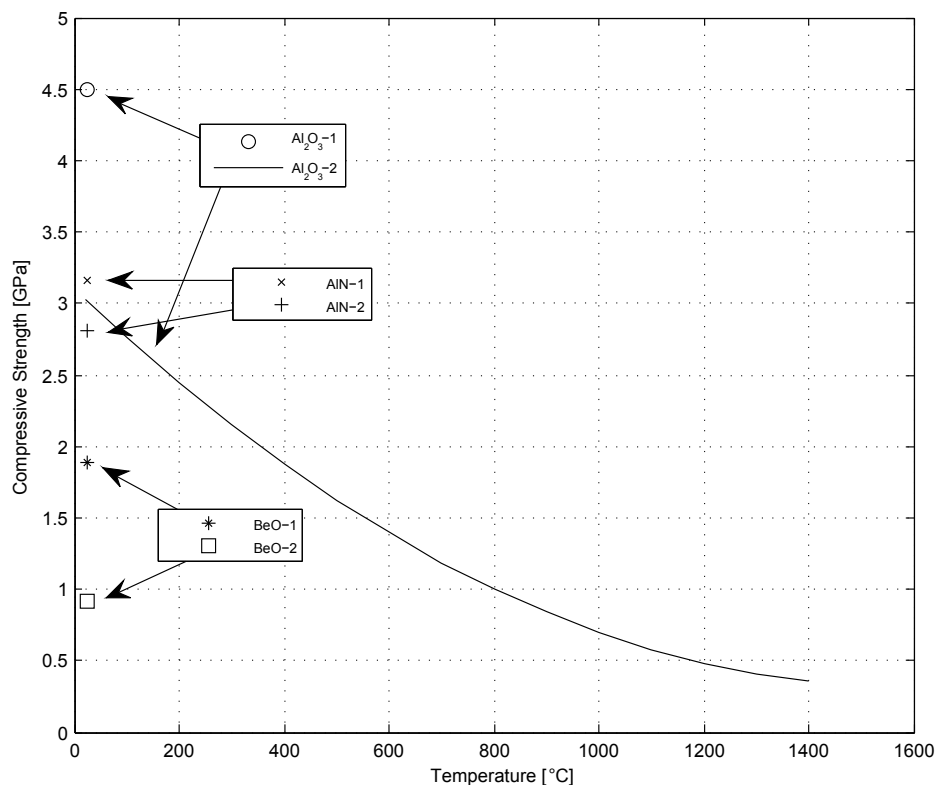


Fig. 8 Compressive strength values from the following references: Al₂O₃-1, hot pressed Al₂O₃ [60]; Al₂O₃-2, review of alumina [17]; AlN-1, hot pressed AlN [60]; AlN-2, hot pressed AlN [167]; BeO-1, cold pressed & sintered BeO [60]; BeO-2, hot pressed BeO [60].

and extrinsic phonon scattering at defects, grain boundaries, and other crystal imperfections, which is approximately independent of temperature [177]. At very low temperatures, phonon-phonon scattering is negligible, resulting in λ scaling with \bar{c}_V , which scales as T_{abs}^3 . At low temperatures the average mean free path is dominated by extrinsic scattering [177]. Phonon-phonon scattering increases with increasing temperature, decreasing the phonon mean free path [177]. The thermal conductivity thus reaches a maximum at low temperatures, typically 30–150 K, and thereafter decreases with increasing temperature. At room temperatures, phonon scattering at grain boundaries is negligible, and is dominated by scattering at crystal lattice imperfections such as dislocations and point defects [110, 178]. At intermediate temperatures, phonon-phonon interactions become the dominant factor in determining the thermal conductivity in ceramics, as phonon-phonon scattering increases with temperature [177]. At high temperature \bar{c}_V approaches a constant value—the Dulong-Petit limit—but the mean free path due to phonon-phonon scattering decreases exponentially, approximately scaling by $1/T_{\text{abs}}$, causing the thermal conductivity to scale approximately with $1/T_{\text{abs}}$ [176, 179], or thermal resistivity to be linearly dependent upon T_{abs} . Deviations from $1/T_{\text{abs}}$ scaling have however been noted for some materials [58]. At very high temperatures the effect of thermal radiation within ceramics becomes important, becoming very significant above 1500 K [180]. At these very high temperatures the thermal conductivity can ap-

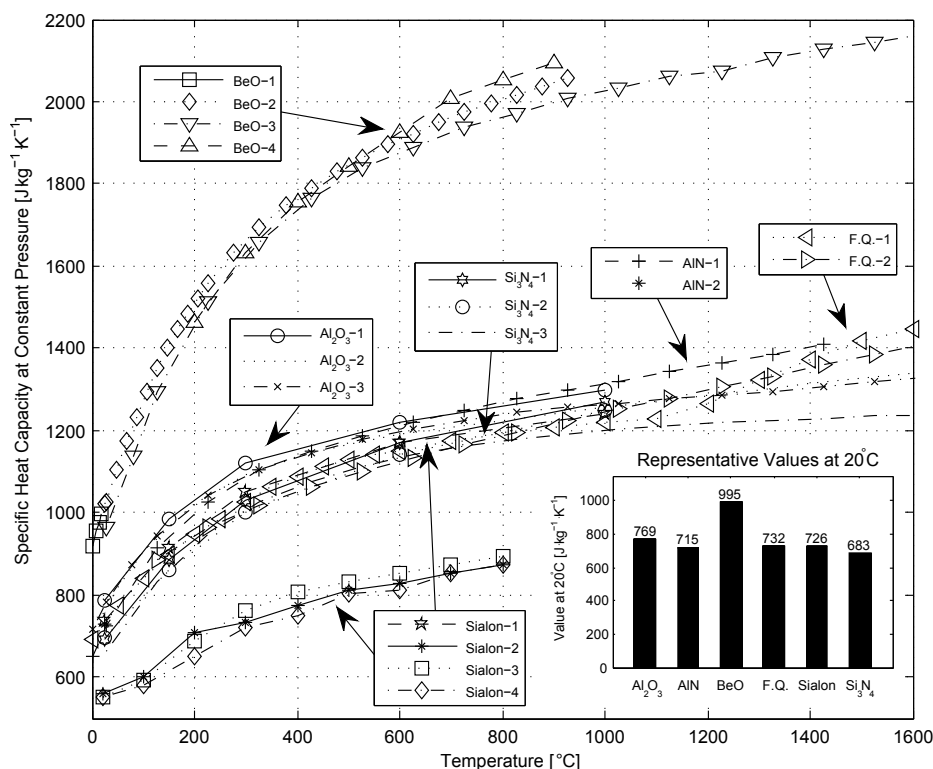


Fig. 9 Specific heat capacity values from the following references: Al_2O_3 -1, CoorsTek AD995 alumina [100]; Al_2O_3 -2, review of alumina [17]; Al_2O_3 -3, review of alumina [170]; AlN-1, theoretical calculation for AlN [144]; AlN-2, theoretical calculation for AlN [171]; BeO-1, 99.6% pure BeO [172]; BeO-2, 99.96% pure BeO [173]; BeO-3, theoretical calculation for BeO [174]; BeO-4, beryllia [175]; F.Q.-1, review of vitreous silica [99]; F.Q.-2, review of vitreous silica [168]; Sialon-1, Kennametal TK4 sialon [100]; Sialon-2, 100 wt% β -sialon [78]; Sialon-3, 5 wt% α -, 95 wt% β -sialon [78]; Sialon-4, 20 wt% α -, 80 wt% β -sialon [78]; Si_3N_4 -1, Ceradyne Ceralloy 147-31N silicon nitride [100]; Si_3N_4 -2, Kyocera SN235P silicon nitride [100]; Si_3N_4 -3, theoretical calculation for β - Si_3N_4 [90].

proach a constant or even increase [180]. For ceramics, large scatter exists in reported values of room temperature thermal conductivity, due to sensitivity of RT thermal conductivity to variations in composition, impurity levels, processing, resulting microstructure [177], and measurement method [180]. The scatter for each material progressively reduces at elevated temperatures, as intrinsic phonon scattering mechanisms controlling thermal conductivity become more dominant, leading to a reduction in sensitivity of thermal conductivity to microstructural or compositional differences [177].

Presence of porosity significantly reduces the RT thermal conductivity of ceramics, due to a reduction in conduction pathways. Thermal conductivity decreases with increasing porosity. Several relations have been proposed to extrapolate thermal conductivity measurements to thermal conductivity at zero porosity, including that of Kingery *et al.* [181]:

$$\lambda_0 = \frac{\lambda_{\text{meas}}}{1 - P} \quad (21)$$

where P is the porosity (pore volume fraction), λ_{meas} is the measured thermal conductivity and λ_0 is the calculated thermal conductivity for zero porosity. However, the relationship between conductivity and porosity is non-linear, and Equation 21 cannot be used over large variations in porosity [58]. RT thermal conductivity can also be reduced by presence of thick, or low thermal conductivity grain boundary phases, or by grain defects.

The thermal conductivity of sintered or hot pressed alumina is lower than that of single crystal alumina (sapphire), with thermal conductivity decreasing with increasing porosity. Typical RT thermal conductivity of sintered Al_2O_3 with $\geq 98\%$ td and $\geq 99.5\%$ purity, is $\approx 32 \text{ W}\cdot\text{m}^{-1}\cdot\text{K}^{-1}$ (compared to $\approx 42 \text{ W}\cdot\text{m}^{-1}\cdot\text{K}^{-1}$ typical for sapphire [101]).

At room temperature, oxygen-related defects are the dominant mechanism limiting the thermal conductivity of AlN [22,40], but their effect decreases at elevated temperatures [24]. Metallic impurities also have the effect of greatly reducing the RT thermal conductivity [38]. Above 1000 K thermal conductivity is governed by anharmonicity [182], leading to the high-temperature thermal conductivity of AlN being independent of ceramic purity. Due to the high dependency upon oxygen-related defects, a wide spread exists in the data reported for RT thermal conductivity of AlN. The thermal conductivity of AlN hot pressed without additives is comparatively low—typically in the range $30\text{--}70 \text{ W}\cdot\text{m}^{-1}\cdot\text{K}^{-1}$ [25, 37]—due to the effects of lattice defects (Al vacancies) resulting from dissolved oxygen impurity. For a given oxygen impurity level, the type and amount of sintering aid added has the greatest effect on AlN thermal conductivity [25].

Yttria, the most commonly used sintering aid for AlN, and other rare-earth oxides, including Sm_2O_3 , Nd_2O_3 and Pr_2O_3 , have been shown to produce near-theoretical density AlN, with high thermal conductivity [25]. The sintering aid CaO has been shown to produce lower thermal conductivity AlN but has a reduced powder cost [183]. The thermal conductivity of yttria-doped AlN increases with dopant addition, as yttria reacts with oxygen to reduce the defect concentration in AlN grains, up to a peak thermal conductivity value [25]. With even greater yttria addition, the increasing yttrium aluminate grain boundary phase thickness reduces the bulk thermal conductivity. Achievement of high thermal conductivity thus requires optimisation of the amount of sintering aid added, with addition of an approximately equimolar amount of Y_2O_3 to the Al_2O_3 content of the AlN powder, resulting in very high thermal conductivity [25]. The thermal conductivity of AlN doped with rare-earth oxides has also been shown to increase with annealing: increasing with longer annealing times and higher annealing temperatures, with an attendant increase in grain size [25].

Irradiation of AlN at room temperature with ultraviolet light has been shown to reversibly reduce its thermal conductivity due to increased phonon scattering cross section, the original thermal conductivity returning when irradiated with visible light [184, 185]. The inner surface of the GCT will be exposed to high levels of UV radiation from the helicon plasma during operation. However, the effect, which is inversely related to sample thickness, becomes negligible for structurally-sized components, and is thus neglected in this study.

For AlN, due to the scarcity of high-temperature experimental measurements of thermal conductivity, a simple extrapolation up to 1400°C may be made using $1/T_{\text{abs}}$ scaling.

Beryllia exhibits the highest RT thermal conductivity of any ceramic, although this decreases rapidly above room temperature, dropping below that of AlN at intermediate temperatures. At very high temperatures a slight increase in thermal conductivity of BeO has been measured [58].

Theoretical analysis of the thermal conductivity of fused quartz—which increases above room temperature in a non-linear manner, in contrast to (crystalline) ceramics—has proved difficult [186]. Radiation heat transfer becomes significant in the measurement of thermal conductivity of fused quartz above $\approx 300^\circ\text{C}$ [169]. The compound effects of conduction and

radiation through the material may be considered as one, as the *effective* thermal conductivity λ^* , or the effects of radiation may be corrected for, yielding the *true* thermal conductivity λ . A divergence thus exists for reported literature values around this temperature, which becomes very significant at high temperatures, with different studies variously reporting the real or effective thermal conductivity [186]. The radiant component of heat transfer varies with sample thickness—resulting in higher measured values of λ^* in thicker samples—and composition [169]. In addition, determination of the correct values of thermal conductivity for fused quartz is complicated by the fact that, despite the large number of experimental studies, few of these specify the origin or purity of the samples tested [99, 169].

α' -sialon has lower thermal conductivity than β' -sialon due to shorter phonon mean free path, resulting from greater lattice asymmetry, and complexity resulting from inclusion of metal cations [78]. Duophase ($\alpha'+\beta'$)-sialons have thermal conductivities intermediate to those of α' -sialon and β' -sialon, with thermal conductivity increasing with β' -phase content [78].

β - Si_3N_4 has high intrinsic thermal conductivity [177, 178, 187–190], with reported thermal conductivities for β - Si_3N_4 as high as $162 \text{ W}\cdot\text{m}^{-1}\cdot\text{K}^{-1}$ [191]. The intrinsic thermal conductivity of α - Si_3N_4 is lower than that of β - Si_3N_4 , due to the higher complexity of its crystal structure [189], with thermal conductivity of silicon nitride ceramics increasing with increasing β -phase content [91, 192].

Selection of type and concentration of additive greatly affects the thermal conductivity and porosity of sintered Si_3N_4 . Typical sintering aids used for the densification of silicon nitride are yttria, alumina and magnesia, and rare-earth oxides either singly or in combination [193], with yttria being found to be effective in producing higher thermal conductivity silicon nitride [91]. The presence of Al ions as impurity or additive affects the thermal conductivity, by Al and O ions forming a solid solution— β' -sialon—in the β - Si_3N_4 grains, leading to increased phonon scattering and thus lower thermal conductivity [177, 192], causing silicon nitride produced with Al_2O_3 sintering aid to have low thermal conductivity. Y_2O_3 or MgO dopants form only secondary phases, and not solid solutions in the Si_3N_4 grains [177], leading to higher sintered thermal conductivities than with Al_2O_3 addition.

Thick glassy grain boundaries can reduce the thermal conductivity of silicon nitride, due to the lower thermal conductivity of the glassy phase, but for silicon nitrides with low secondary phase content, grain boundary thickness is not the main controlling factor on thermal conductivity [91].

Room temperature thermal conductivity of silicon nitride is not controlled by grain size, with large increases in grain size only slightly increasing the thermal conductivity [110], particularly for Al_2O_3 -doped Si_3N_4 [91]. Instead, the RT thermal conductivity is controlled by the amount of structural defects, such as dislocations and point defects, which cause phonon scattering [91]. Although high thermal conductivities have been reported for Y_2O_3 -doped Si_3N_4 with large β - Si_3N_4 grains [194, 195], the higher thermal conductivity is due to reduced structural defect density in the larger grains [91]. The thermal conductivity of β - Si_3N_4 crystals is anisotropic [196]. Very high (and macroscopically anisotropic) thermal conductivities have been achieved for silicon nitrides with large oriented elongated β -phase grains, resulting from anisotropic processing techniques (extrusion [191], hot pressing [110], tape-casting [178, 197]), and in some cases by also seeding with β - Si_3N_4 crystals.

Processing details, including sintering temperature [91] also strongly affect the resultant microstructure, and thus the thermal conductivity. Attainment of high thermal conductivity requires the use of high purity starting powders with low oxygen content and low cationic impurities, full densification of the sintered body, and the optimisation of many factors including sintering parameters [91] and sintering aid(s). Very high thermal conductivity Si_3N_4

has been reported in many studies [94, 191, 198–200], produced by careful control of purity and oxygen content of raw powders [94, 201], selection of additives [202], control of microstructure morphology and grain size [109, 178, 194, 197, 203, 204], and use of β - Si_3N_4 seed crystals [205]. However, despite the large volume of studies reporting techniques for production of high thermal conductivity silicon nitride, typical commercially available silicon nitride [206] at present has a far lower thermal conductivity. As the thermal conductivity of these experimental materials does not reflect what is commercially available, they will not be considered for the purposes of determining the most representative set of commercially available material values in the current analysis. Si_3N_4 with thermal conductivities in excess of $45 \text{ W}\cdot\text{m}^{-1}\cdot\text{K}^{-1}$ are not commonly commercially available, typical values being in the range $15\text{--}42 \text{ W}\cdot\text{m}^{-1}\cdot\text{K}^{-1}$. Typical high-purity commercial Si_3N_4 powders contain $\approx 1 \text{ wt}\%$ oxygen [94], and metallic impurities [91], limiting the attainable thermal conductivity. The coarse microstructures typically present in high thermal conductivity Si_3N_4 , resulting from promotion of grain growth, significantly impacts on the material's strength [94, 110, 207], reducing the suitability of these materials for structural applications. Although these materials are not typically commercially available, the volume of ongoing research in this field will likely lead to these high thermal conductivity materials becoming commercially available in the coming years, broadening the spectrum of applications for silicon nitride.

4.3 Thermal Expansion Coefficient

Accurate knowledge of thermal expansion coefficients at elevated temperatures is critical for material processing [210] and prediction of thermal stresses for mechanical design. The rate of change of specific volume of most materials typically increases with increasing temperature [210], leading to increasing issues of thermal stress at elevated temperatures. The dilation of a material with temperature may be characterised by the rate of change of a linear dimension of the material, referred to the instantaneous length of that dimension, termed the *true instantaneous* coefficient of thermal expansion (COTE), α' such that:

$$\alpha' = \frac{1}{L_T} \frac{\partial L}{\partial T} \quad (22)$$

where L_T is the length of the specimen at temperature T . A more commonly used procedure [99] is to express thermal dilation as the rate of change of linear dimension with temperature, referred to the specimen's linear dimension at some reference temperature, such as 0°C or 25°C :

$$\alpha = \frac{1}{L_0} \frac{\partial L}{\partial T} \quad (23)$$

where L_0 is the linear dimension at the reference temperature. As the absolute change in dimension of the specimen will be very small, the instantaneous COTE referred to a reference temperature (α) will be an excellent approximation to the true instantaneous COTE (α'). Thermal dilation is also commonly expressed as an average coefficient of thermal expansion between a reference temperature, such as 0°C or 25°C , and a specified higher temperature:

$$\bar{\alpha} = \frac{1}{L_0} \frac{L - L_0}{T - T_0} \quad (24)$$

where L_0 is the linear dimension at the reference temperature T_0 . Care must be taken when dealing with COTE data, to distinguish between values of instantaneous and average COTE.

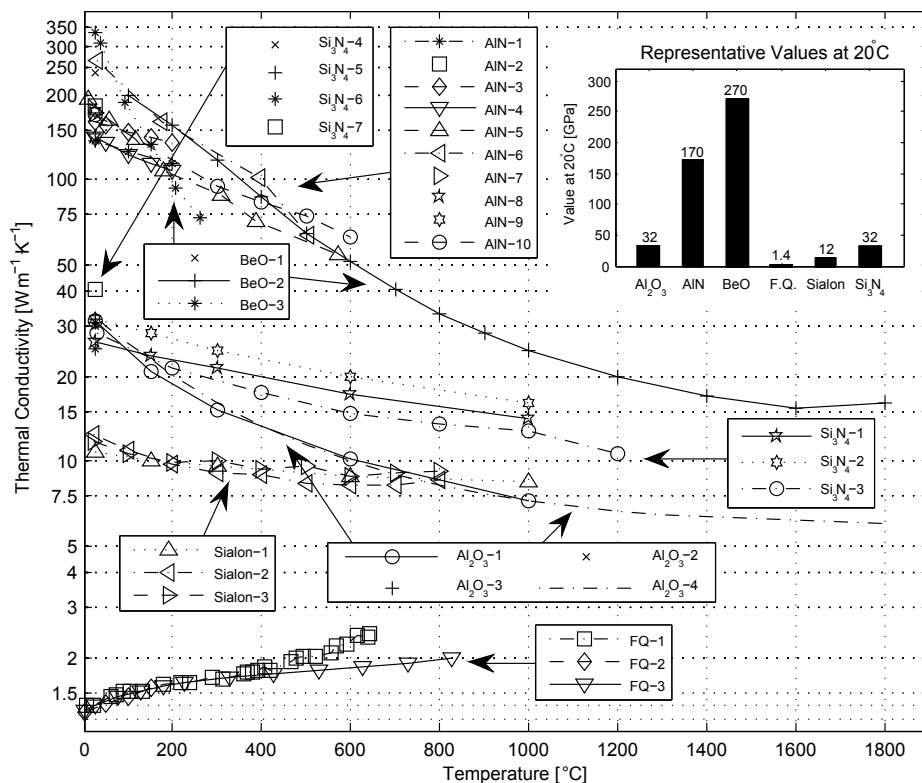


Fig. 10 Thermal conductivity values. Al₂O₃-1, CoorsTek AD995 alumina [100]; Al₂O₃-2, CoorsTek AD998 alumina [101]; Al₂O₃-3, Wesgo AL998 alumina [101]; Al₂O₃-4, review of alumina [17]; AlN-1, tape cast, dry-pressed & sintered AlN [27]; AlN-2, sintered AlN 2.9 wt% Y₂O₃ [44]; AlN-3, hot pressed AlN substrate [26]; AlN-4, sintered AlN substrate [26]; AlN-5, sintered AlN, 2.2 wt% oxygen impurity [182]; AlN-6, sintered AlN, 0.05 wt% oxygen impurity [182]; AlN-7, sintered AlN 5 wt% Y₂O₃, 0.8 wt% O [156]; AlN-8, sintered AlN 1 mol% Y₂O₃ [103]; AlN-9, sintered AlN 4.91 wt% Y₂O₃ [25]; AlN-10, sintered AlN 4 wt% Y₂O₃ [25]; BeO-1, Brush-Wellman 995 BeO [101]; BeO-2, 95%t.d. BeO [58]; BeO-3, sintered un-doped BeO, 2.86 g·cm⁻³ [52]; F.Q.-1, 99.97% pure fused quartz [186]; F.Q.-2, fused quartz [208]; F.Q.-3, review of fused quartz [169]; Sialon-1, Kennametal TK4 sialon [100]; Sialon-2, β-sialon [78]; Sialon-3, 20% α-, 80% β-sialon [78]; Si₃N₄-1, Ceradyne Ceralloy 147-31N silicon nitride [100]; Si₃N₄-2, Kyocera SN235P silicon nitride [100]; Si₃N₄-3, nitrided pressureless sintered silicon nitride [209]; Si₃N₄-4, Ceramic For Industry CFI3208 silicon nitride [206]; Si₃N₄-5, Kyocera SN235P silicon nitride [206]; Si₃N₄-6, Honeywell GS44 silicon nitride [206]; Si₃N₄-7, Honeywell AS800 silicon nitride [206].

Thermal dilation may also be more fundamentally defined in terms of rate of change of volume with respect to temperature, with corresponding definitions for volumetric true instantaneous COTE, instantaneous COTE referred to a reference temperature, and average COTE respectively:

$$\beta' = \frac{1}{V_T} \frac{\partial V}{\partial T} \quad (25)$$

$$\beta = \frac{1}{V_0} \frac{\partial V}{\partial T} \quad (26)$$

$$\bar{\beta} = \frac{1}{V_0} \frac{V - V_0}{T - T_0} \quad (27)$$

In experimental studies of thermal expansion of ceramics found in the literature, linear coefficients of expansion are more widely reported than volumetric coefficients, as linear variations in specimen dimension can be more easily measured than volumetric variations; although volumetric coefficients of thermal expansion are commonly found in the literature for computational physics studies of the structure of materials. For isotropic substances, the instantaneous linear COTE may be approximated by $\alpha \cong \beta/3$ with only a small error, as the actual linear dilation will be small. Data from some sources reported as values of instantaneous volumetric COTE have been used in this study, by utilising this approximate relation. The rate of dilation of ceramics with respect to temperature is relatively independent of porosity, allowing thermal expansion coefficients to be calculated from lattice parameter measurements [211], with only slight error resulting from defects in the polycrystalline material [17]. The thermal expansion coefficient of non-cubic crystals is typically anisotropic [210], resulting in change in both shape (deformation) and volume (dilation) when heated [99]. Anisotropic thermal expansion of non-cubic lattice structures in polycrystalline materials can lead to thermal-stress-induced-cracking [210]. For crystals of the hexagonal lattice system the instantaneous thermal expansion coefficients along the a and c lattice directions are defined by:

$$\alpha_a = \frac{1}{a_T} \frac{\partial a}{\partial T} \approx \frac{1}{a_0} \frac{\partial a}{\partial T} \quad (28)$$

$$\alpha_c = \frac{1}{c_T} \frac{\partial c}{\partial T} \approx \frac{1}{c_0} \frac{\partial c}{\partial T} \quad (29)$$

The directionally averaged instantaneous thermal expansion coefficient of the corresponding polycrystalline material composed of randomly oriented grains is then:

$$\tilde{\alpha} = \frac{(2\alpha_a + \alpha_c)}{3} \quad (30)$$

Data from both X-ray diffraction of single-crystals and dilatometry are considered for the determination of the instantaneous linear COTE of the ceramics considered in this study. The amorphous nature of fused quartz necessitates the sole use of dilatometry. For substances with the wurtzite crystal structure, such as AlN and BeO, α_c is lower than α_a , leading to a reduction in the c/a ratio with increasing temperature [145, 210, 212]. Some polycrystalline ceramics exhibit preferential grain orientation, typically resulting from processing such as extrusion, hot pressing or tape-casting, leading to macroscopically anisotropic thermal expansion. BeO ceramics have been variously reported with macroscopically isotropic [58] and anisotropic [59] thermal expansion coefficients. The COTE of many but not all specimens of vitreous silica reported are very slightly anisotropic [99]. Due to the high purity of fused quartz, its thermal expansion coefficient can be significantly affected by small differences in composition [65]. The previous thermal history of a sample of fused quartz can greatly affect its measured thermal expansion coefficient, with significant differences noted between un-annealed and fully annealed samples [65, 99]. The α' and β' -phases of sialon have differing thermal expansion coefficients ($\alpha_{\alpha'\text{-phase}} \approx 3.7\text{--}4.0 \times 10^{-6} \text{ K}^{-1}$ [71], $\alpha_{\beta'\text{-phase}} \approx 3.2 \times 10^{-6} \text{ K}^{-1}$), causing residual stresses to develop in duophase sialons [75]. The thermal expansion coefficient of oxynitride glass ($\alpha \approx 5.2\text{--}6.6 \times 10^{-6} \text{ K}^{-1}$) differs from that of both α' and β' -sialon phases—affecting the bulk properties of the ceramic—and is dependent upon various factors, including nitrogen content and modifier cation, increasing N:O ratio resulting in a decrease in thermal expansion coefficient due to increased cross-linking [79]. The thermal expansion coefficients of the α and β -phases of Si_3N_4 differ by only a very small amount [90].

Temperature-dependent data for the thermal expansion coefficients of all materials are given in Figure 11.

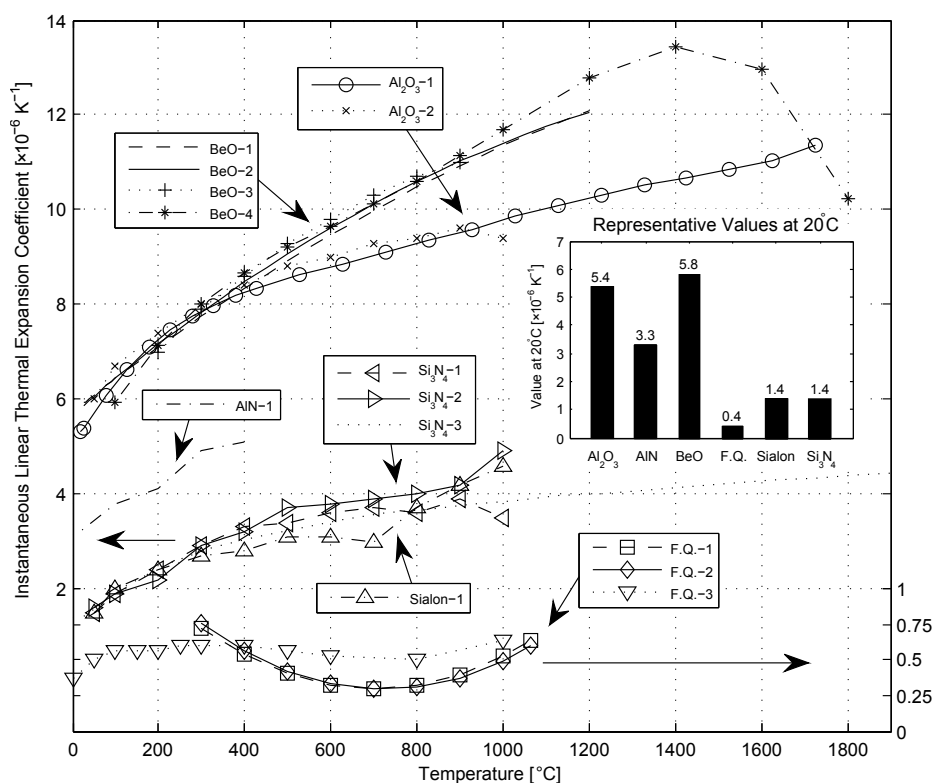


Fig. 11 Thermal expansion coefficient values from the following references: Al_2O_3 -1, review of alumina [170]; Al_2O_3 -2, CoorsTek AD995 alumina [100]; AlN-1, hot pressed AlN [26]; BeO-1, isostatically pressed & sintered BeO [59]; BeO-2, extruded & sintered BeO [59]; BeO-3, review of BeO [175]; BeO-4, review of BeO [58]; F.Q.-1, fused quartz from electrically melted quartz crystal powder [65]; F.Q.-2, fused quartz from flame fusion of quartz crystals [65]; F.Q.-3, review of vitreous silica [99]; Sialon-1, Kennametal TK4 sialon [100]; Si_3N_4 -1, Ceradyne Ceralloy 147-31N silicon nitride [100]; Si_3N_4 -2, Kyocera SN235P silicon nitride [100]; Si_3N_4 -3, theoretical calculation β - Si_3N_4 [90];

5 Conclusions

Representative material property data, given as a function of temperature where possible, have been gathered for constrained material specifications for alumina, aluminium nitride, beryllia, fused quartz, sialon and silicon nitride. The material specifications have been chosen to best reflect advanced commercially available material grades. These data can be used by the design engineer in the preliminary stages of design for materials selection and simulation. Detailed design should always be supported by experimental verification of the material properties of the intended material.

It is clear from this study that more experimental studies of the tensile, flexural and compressive strengths are required as a function of temperature, for candidate structural ceramics for use in high power plasma sources and other high power dielectric applications. Further work is required to compile representative values for the dielectric properties of these materials, and to assess the resistance of these materials to the plasma environment in VASIMR®.

Acknowledgements The authors would like to acknowledge the financial support of the FÁS Science Challenge Programme, Ireland.

References

1. F. R. Chang-Diaz. The VASIMR rocket. *Scientific American*, 283(5):90–97, 2000.
2. JP Squire, FR Chang-Diaz, TW Glover, VT Jacobson, GE McCaskill, DS Winter, FW Baity, MD Carter, and RH Goulding. High power light gas helicon plasma source for VASIMR. *Thin Solid Films*, 506:579–582, May 2006.
3. O. Batishchev, K. Molvig, F. R. Chang-Diaz, and J. P. Squire. Study of gas burn-out regime in the VASIMR helicon plasma source. In *30th EPS Conference on Controlled Fusion and Plasma Physics, St. Petersburg, Russia, 7-11 July, 2003*.
4. K. T. Stanton, D. J. Browne, and J. Mulcahy. Thermal management strategies for VASIMR. High Power Electrical Propulsion Workshop, Ad Astra Rocket Company, Liberia, Costa Rica, July 17th, 2006.
5. J. M. Mulcahy, D. J. Browne, K. T. Stanton, F. R. Chang-Diaz, and L. Cassady. Use of thermocouple and infrared camera data to compute helicon plasma source heat flux using inverse method. In *5th European Thermal-Sciences Conference, The Netherlands, 2008*.
6. James M. Mulcahy, David J. Browne, Kenneth T. Stanton, Franklin R. Chang Diaz, Leonard D. Cassady, Daniel F. Berisford, and Roger D. Bengtson. Heat flux estimation of a plasma rocket helicon source by solution of the inverse heat conduction problem. *International Journal of Heat and Mass Transfer*, 52(9-10):2343–2357, Apr 2009.
7. T Tanikawa and S Shinohara. Plasma performance in very large helicon device. *Thin Solid Films*, 506:559–563, May 2006.
8. G. S. Fu, H. J. Xu, S. F. Wang, W. Yu, W. Sun, and L. Han. Epitaxial growth of ZnO films by helicon-wave-plasma-assisted sputtering. *Physica B: Condensed Matter*, 382(1-2):17–20, Jun 2006.
9. D. D. Blackwell and F. F. Chen. Two-dimensional imaging of a helicon discharge. *Plasma Sources Science & Technology*, 6(4):569–576, Nov 1997.
10. K Toki, S Shinohara, T Tanikawa, and KP Shamrai. Small helicon plasma source for electric propulsion. *Thin Solid Films*, 506:597–600, May 2006.
11. H. Chen, E. Kallos, P. Muggli, T. C. Katsouleas, and M. A. Gundersen. A high-density hydrogen-based capillary plasma source for particle-beam-driven Wakefield accelerator applications. *Plasma Science, IEEE Transactions on*, 37(3):456–462, Mar 2009.
12. C.E. Little. Pulsed metal-vapour lasers. In *Gas Discharges as Coherent and Incoherent Light Sources, IEE Colloquium on*, 1990.
13. D G Loveland, D A Orchard, A F Zerrouk, and C E Webb. Design of a 1.7 W stable long-lived strontium vapour laser. *Measurement Science and Technology*, 2(11):1083, 1991.
14. David Heemstra and Kevin White. Rupture resistant plasma tube, 2010. U.S.A. Patent No. 7759600. Filed 2006. Samsung Austin Semiconductor, L.P., Samsung Electronics Co., Ltd.
15. Maria Huffman, Palanikumar Sakthivel, Teresa Zimmerman, and Thomas Noble. Fluorine assisted stripping and residue removal in sapphire downstream plasma asher, 2000. U.S.A. Patent No. 6082374. Filed 1997.
16. W. A. Weibull. A statistical distribution function of wide applicability. *Journal of Applied Mechanics - Transactions of the ASME*, 18(3):293–297, 1951.
17. RG Munro. Evaluated material properties for a sintered alpha-alumina. *Journal of the American Ceramic Society*, 80(8):1919–1928, Aug 1997.
18. W. Borland. *Electronic Materials Handbook: Packaging*, volume 1, chapter Thick-Film Hybrids, pages 332–353. ASM International, 1989.
19. JA Heikkinen, S Orivuori, J Linden, S Saarelma, and L Heikinheimo. Thermal and electrical analysis of alumina and beryllia coax high-power windows under irradiation. *IEEE Transactions on Dielectrics and Electrical Insulation*, 6(2):169–174, Apr 1999.
20. MMR Howlader, C Kinoshita, K Shiiyama, and M Kutsuwada. Electrical conductivity of Wesgo AL995 alumina under fast electron irradiation in a high voltage electron microscope. *Journal of Applied Physics*, 92(4):1995–1999, Aug 2002.
21. R. H. Goulding, S. J. Zinkle, D. A. Rasmussen, and R. E. Stoller. Transient effects of ionizing and displacive radiation on the dielectric properties of ceramics. *Journal of Applied Physics*, 79(6):2920–2933, Mar 1996.
22. Glen A. Slack, R. A. Tanzilli, R. O. Pohl, and J. W. Vandersande. The intrinsic thermal conductivity of AlN. *Journal of Physics and Chemistry of Solids*, 48(7):641 – 647, 1987.

23. Masahide OKAMOTO, Hideo ARAKAWA, Masabumi OOHASHI, and Satoru OGIHARA. Effect of microstructure on thermal conductivity of AlN ceramics. *Journal of the Ceramic Society of Japan*, 97(1132):1478–1485, 1989.
24. K Watari, H Nakano, K Urabe, K Ishizaki, SX Cao, and K Mori. Thermal conductivity of AlN ceramic with a very low amount of grain boundary phase at 4 to 1000 K. *Journal of Materials Research*, 17(11):2940–2944, Nov 2002.
25. TB Jackson, AV Virkar, KL More, RB Dinwiddie, and RA Cutler. High-thermal-conductivity aluminum nitride ceramics: The effect of thermodynamic, kinetic, and microstructural factors. *Journal of the American Ceramic Society*, 80(6):1421–1435, Jun 1997.
26. Y. Kurokawa, K. Utsumi, H. Takamizawa, T. Kamata, and S. Noguchi. Aln substrates with high thermal conductivity. *Components, Hybrids, and Manufacturing Technology, IEEE Transactions on*, 8(2):247 – 252, Jun 1985.
27. N. Kuramoto, H. Taniguchi, and I. Aso. Translucent AlN ceramic substrate. *Components, Hybrids, and Manufacturing Technology, IEEE Transactions on*, 9(4):386 – 390, Dec 1986.
28. F. Miyashiro, N. Iwase, A. Tsuge, F. Ueno, M. Nakahashi, and T. Takahashi. High thermal conductivity aluminum nitride ceramic substrates and packages. *Components, Hybrids, and Manufacturing Technology, IEEE Transactions on*, 13(2):313 – 319, Jun 1990.
29. M.G. Norton. Characterisation of aluminium nitride ceramic substrates. *Microelectronics International*, 6(3):18–22, 1993.
30. M. T. Gosey, K. J. Lodge, and E. A. Logan. Aluminium nitride for packaging high performance electronic circuits. *GEC Journal of Research*, 8(3):137–144, 1991.
31. Jonathan Harris. Sintered aluminum nitride ceramics for high-power electronic applications. *JOM Journal of the Minerals, Metals and Materials Society*, 50(6):56–60, 1998.
32. K.J. Lodge, J.A. Sparrow, E.D. Perry, E.A. Logan, M.T. Goosey, D.J. Pedder, and C. Montgomery. Prototype packages in aluminum nitride for high performance electronic systems. *Components, Hybrids, and Manufacturing Technology, IEEE Transactions on*, 13(4):633 – 638, Dec 1990.
33. L. La Spina, E. Iborra, H. Schellevis, M. Clement, J. Olivares, and L. K. Nanver. Aluminum nitride for heatspreading in RF IC's. *Solid-state electronics*, 52(9):1359–1363, Sep 2008.
34. Zhigang Lin and R.J. Yoon. An AlN-based high temperature package for SiC devices: materials and processing. In *Advanced Packaging Materials: Processes, Properties and Interfaces, 2005. Proceedings. International Symposium on*, pages 156 – 159, Mar 2005.
35. G Long and LM Foster. Aluminum nitride containers for synthesis of GaAs. *Journal of the Electrochemical Society*, 109(12):1176–1179, 1962.
36. W. Rafaniello. Development of aluminum nitride: a new low-cost armor. Final report. Technical Report Contract Number DAAL03-88-C-001, U.S. Army Research Office, 2nd Dec 1992.
37. KM TAYLOR and C LENIE. Some properties of aluminum nitride. *Journal of the Electrochemical Society*, 107(4):308–314, 1960.
38. N. Kuramoto, H. Taniguchi, Y. Numata, and I. Aso. Sintering process of translucent AlN and effect of impurities on thermal conductivity of AlN ceramics. *Journal of the Ceramic Association, Japan*, 93(1081):517–522, 1985.
39. F. Ueno, A. Horiguchi, M. Kasori, K. Shinozaki, and A. Tsuge. High thermal conductive aluminium nitride. In *IUPAC-CHEMRAWN VI, Advanced Materials for Innovations in Energy, Transportation and Communications, Tokyo, Japan, 17-22 May, 1987*.
40. J. H. Harris, R. A. Youngman, and R. G. Teller. On the nature of oxygen-related defect in aluminum nitride. *Journal of Materials Research*, 5(8):1763–1773, Aug 1990.
41. H Buhr, G. Muller, H. Wiggers, F. Aldinger, P. Foley, and A. Roosen. Phase-composition, oxygen-content, and thermal-conductivity of AlN(Y2O3) ceramics. *Journal of the American Ceramic Society*, 74(4):718–723, Apr 1991.
42. GA SLACK. Nonmetallic crystals with high thermal-conductivity. *Journal of Physics and Chemistry of Solids*, 34(2):321–335, 1973.
43. GA Slack, LJ Schowalter, D Morelli, and JA Freitas. Some effects of oxygen impurities on AlN and GaN. *Journal of Crystal Growth*, 246(3-4):287–298, Dec 2002.
44. H. Sakai, Y. Katsuda, M. Masuda, C. Ihara, and T. Kameyama. Effects of adding Y2O3 on the electrical resistivity of aluminium nitride ceramics. *Journal of the Ceramic Society of Japan*, 116(4):566–571, 2008.
45. Koji Watari. High thermal conductivity non-oxide ceramics. *Journal of the Ceramic Society of Japan*, 109(1265):S7–S16, 2001.
46. J.P. SACHET, J.Y. LAVAL, F. LEPOUTRE, and A.C. BOCCARA. Thermal behavior of grain boundaries in aluminum nitride ceramics. *Journal de Physique Colloques*, 51(C1):617–622, 1990.
47. S MITRA, G DUTTA, and I DUTTA. Effect of heat-treatment on the microstructure and properties of dense AlN sintered with Y2O3 additions. *Journal of the American Ceramic Society*, 78(9):2335–2344, Sep 1995.

48. T. Schultheiss, V. Christina, M. Cole, J. Rathke, T. Elliott, V. Nguyen, L. Phillips, and J. Preble. A high thermal conductivity waveguide window for use in a free electron laser. In *Particle Accelerator Conference, 1999. Proceedings of the 1999*, volume 2, pages 780–782 vol.2, 1999.
49. P.S. Hessinger, K.H. Styhr, and E. Ryskewitch. Beryllium oxide radome development - final engineering report. Technical report, National Beryllia Corp., Haskell, New Jersey, 1962.
50. L. L. Snead and S. J. Zinkle. Use of beryllium and beryllium oxide in space reactors. In *Space Technology and Applications International Forum - STAIF 2005*, volume 746, pages 768–775, 2005.
51. Craig Hamlyn-Harris, Andrew Borthwick, John Fanthome, Chris Waldon, Mark Nightingale, and Neal Richardson. Engineering design of an RF vacuum window for the ITER ICRH antenna. *Fusion Engineering and Design*, 84(2-6):887–894, Jun 2009.
52. W. W. Beaver, J. G. Theodore, and C. A. Bielawski. Effects of powder characteristics, additives and atmosphere on the sintering of sulfate-derived beo. *Journal of Nuclear Materials*, 14:326–337, 1964.
53. T. E. Clare. Studies in the cold pressing and sintering of beryllia. *Journal of Nuclear Materials*, 14:359–367, 1964.
54. S. C. Carniglia, R. E. Johnson, A. C. Hott, and G. G. Bente. Hot pressing for nuclear applications of BeO; process, product, and properties. *Journal of Nuclear Materials*, 14:378–394, 1964.
55. J. Bardsley and A. Ridal. The development of a technique for extrusion and sintering of beryllia. *Journal of Nuclear Materials*, 14:368–377, 1964.
56. K. Veevers, J.F. Whatham, and W.J. Wright. A study of variables in the mechanical testing of beryllia. *Journal of Nuclear Materials*, 14:395–403, 1964.
57. R. J. Brown and N.W. Bass. Fabrication and properties of commercial beryllia ceramics for nuclear applications. *Journal of Nuclear Materials*, 14:341–348, 1964.
58. J. Lillie. Some properties of beryllium oxide. Technical Report UCRL-6457, Lawrence Radiation Laboratory, University of California, Livermore, California, May 19 1961.
59. R. E. Fryxell and B. A. Chandler. Creep, strength, expansion, and elastic moduli of sintered BeO as a function of grain size, porosity, and grain orientation. *Journal of the American Ceramic Society*, 47(6):283–291, 1964.
60. H. C. Heard and C. F. Cline. Mechanical-behavior of polycrystalline BeO, Al₂O₃ and AlN at high-pressure. *Journal of Materials Science*, 15(8):1889–1897, 1980.
61. J. W. Kelly. The texture of hot-pressed beryllium oxide. *Journal of Nuclear Materials*, 8(2):227–231, 1963.
62. C. S. Alexander, L. C. Chhabildas, W. D. Reinhart, and D. W. Templeton. Changes to the shock response of fused quartz due to glass modification. *International Journal of Impact Engineering*, 35(12):1376–1385, Dec 2008.
63. T. Shikama, K. Yasuda, S. Yamamoto, C. Kinoshita, SJ Zinkle, and ER Hodgson. Irradiation effects in ceramics for fusion reactor applications. *Journal of Nuclear Materials*, 271:560–568, May 1999.
64. A. Gorshkov, D. Orlinski, V. Sannikov, K. Vukolov, S. Goncharov, Y. Sadovnikov, and A. Kirillov. Measurements of the radiation resistant fused quartz radioluminescence spectral intensity under irradiation in the pulse nuclear reactor. *Journal of Nuclear Materials*, 273(3):271–276, Aug 1999.
65. J OISHI and T KIMURA. Thermal expansion of fused quartz. *Metrologia*, 5(2):50–&, 1969.
66. K. H. Jack and W. I. Wilson. Ceramics based on the Si-Al-O-N and related systems. *Nature Physical Science*, 238(80):28–&, 1972.
67. Y OYAMA and KAMIGAITO. Solid solutions of some oxides in Si₃N₄. *Japanese Journal of Applied Physics*, 10(11):1637–&, 1971.
68. K. H. Jack. Nitrogen ceramics. *Transactions and Journal of the British Ceramic Society*, 72(8):376–389, 1973.
69. Y OYAMA. Solid-solution in ternary-system, Si₃N₄-AlN-Al₂O₃. *Japanese Journal of Applied Physics*, 11(5):760–&, 1972.
70. K. H. Jack. Sialons and related nitrogen ceramics. *Journal of Materials Science*, 11(6):1135–1158, 1976.
71. G. Z. Cao and R. Metselaar. α' -sialon ceramics: A review. *Chemistry of Materials*, 3(2):242–252, Mar-Apr 1991.
72. S.A.B. Jama, D.P. Thompson, and K.H. Jack. The lithia-silicon nitride-alumina system. *Special Ceramics*, 6:299–308, 1975.
73. S. Hampshire, H. K. Park, D. P. Thompson, and K. H. Jack. Alpha'-SIALON ceramics. *Nature*, 274(5674):880–882, 1978.
74. N. C. Acikbas, E. Suvaci, and H. Mandal. Fabrication of functionally graded SiAlON ceramics by tape casting. *Journal of the American Ceramic Society*, 89(10):3255–3257, Oct 2006.
75. T. Ekström, L. K. L. Falk, and Z. J. Shen. Duplex alpha,beta-sialon ceramics stabilized by dysprosium and samarium. *Journal of the American Ceramic Society*, 80(2):301–312, Feb 1997.

76. E. Soderlund and T. Ekstrom. Pressureless sintering of Y₂O₃-CeO₂-doped sialons. *Journal of Materials Science*, 25(11):4815–4821, Nov 1990.
77. T. Ekström. Effect of composition, phase content and microstructure on the performance of yttrium sil–al–o–n ceramics. *Materials Science and Engineering: A*, 109:341 – 349, 1989. Proceedings of the Symposium on Ceramic Materials Research.
78. D. M. Liu, C. J. Chen, and R. R. R. Lee. Thermal-diffusivity conductivity in sialon ceramics. *Journal of Applied Physics*, 77(2):494–496, Jan 1995.
79. Stuart Hampshire and Michael J. Pomeroy. Oxynitride glasses. *International Journal of Applied Ceramic Technology*, 5(2):155–163, 2008.
80. N. Çaliş, Ş. R. Kuşhan, F. Kara, and H. Mandal. Functionally graded SiAlON ceramics. *Journal of the European Ceramic Society*, 24(12):3387–3393, 2004.
81. W. D. Carruthers, P. F. Becher, M. K. Ferber, and J. Pollinger. Advances in the development of silicon nitride and other ceramics. In *Proceedings of ASME Turbo Expo*, Amsterdam, The Netherlands, June 3-6 2002.
82. ZJ Shen, H Peng, P Pettersson, and M Nygren. Self-reinforced alpha-SiAlON ceramics with improved damage tolerance developed by a new processing strategy. *Journal of the American Ceramic Society*, 85(11):2876–2878, Nov 2002.
83. A. K. Woodruff and J. Hellmann. Characterization of long SiAlON ceramic tubes for gun barrel applications. Technical Report ARL-CR-573, Army Research Laboratory, Aberdeen Proving Ground, MD, U.S.A., Jun 2006.
84. XL Su, PL Wang, WW Chen, B Zhu, YB Cheng, and DS Yan. Translucent alpha-sialon ceramics by hot pressing. *Journal of the American Ceramic Society*, 87(4):730–732, Apr 2004.
85. I Zalite, N Zilinska, and G Kladler. Some sialons prepared from nanopowders by hot pressing. *Journal of Physics: Conference Series*, 93(1):012008, 2007.
86. K.H. Jack. *Non-Oxide Technical and Engineering Ceramics*, chapter Sialons: A Study in Materials Development, pages 1–30. Elsevier Applied Science Publishers Ltd., London, 1986.
87. K.W. Kirby, A. Jankiewicz, M. Janney, C. Walls, and D. Kupp. Gelcasting of GD-1 ceramic radomes. In *Proceedings of the 8th DoD Electromag. Windows Symposium*, pages 287–295, 2000.
88. D. Hardie and K. H. Jack. Crystal structures of silicon nitride. *Nature*, 180(4581):332–333, 1957.
89. R. Grün. Crystal structure of beta-Si₃N₄ - structural and stability considerations between alpha-Si₃N₄ and beta-Si₃N₄. *Acta Crystallographica Section B: Structural Science*, 35:800–804, 1979.
90. Akihide Kuwabara, Katsuyuki Matsunaga, and Isao Tanaka. Lattice dynamics and thermodynamical properties of silicon nitride polymorphs. *Physical Review B*, 78(6):064104, Aug 2008.
91. K. Watari, K. Hirao, M. E. Brito, M. Toriyama, and K. Ishizaki. Factors to enhance thermal conductivity of β -Si₃N₄ ceramics. *Advances in Technology of Materials and Materials Processing Journal*, 7(2):191–202, 2005.
92. K. Suganuma. *Joining of Ceramics*, chapter Joining Silicon Nitride to Metals and to Itself, pages 173–193. Chapman and Hall, London, 1990.
93. K. Hayashi, S. Tsujimoto, T. Nishikawa, and Y. Imamura. Thermal conductivity of reaction bonded Si₃N₄. *Journal of the Ceramic Association, Japan*, 94(6):595–600, 1986.
94. You Zhou, Xinwen Zhu, Kiyoshi Hirao, and Zoltan Lencses. Sintered reaction-bonded silicon nitride with high thermal conductivity and high strength. *International Journal of Applied Ceramic Technology*, 5(2):119–126, 2008.
95. Frantisek Lofaj and Sheldon N. Wiederhorn. Creep processes in silicon nitride ceramics. *Journal of ceramic processing research*, 10(3):269–277, Jun 2009.
96. SM Wiederhorn, RF Krause, F Lofaj, and U Taffner. Creep behavior of improved high temperature silicon nitride. In HD Kim, HT Lin, and MJ Hoffmann, editors, *Advanced Si-based ceramics and composites*, volume 287 of *Key Engineering Materials*, pages 381–392. Trans Tech Publications Ltd, 2005.
97. G Ling and HT Yang. Pressureless sintering of silicon nitride with magnesia and yttria. *Materials Chemistry and Physics*, 90(1):31–34, Mar 2005.
98. S. P. Dodd, G. A. Saunders, M. Cankurtaran, and B. James. Ultrasonic study of the elastic and nonlinear acoustic properties of ceramic aluminum nitride. *Journal of Materials Science*, 36(3):723–729, Feb 2001.
99. R. B. Sosman. *The Properties of Silica*. American Chemical Society Monograph Series (No. 37), Book Department, The Chemical Catalog Company, Inc., New York, 1927.
100. J. J. Swab, A. A. Wereszczak, J. Tice, R. Caspe, R. H. Kraft, and J. W. Adams. Mechanical and thermal properties of advanced ceramics for gun barrel applications. Technical Report ARL-TR-3417, Army Research Laboratory, 2005.
101. LL Snead, SJ Zinkle, and DP White. Thermal conductivity degradation of ceramic materials due to low temperature, low dose neutron irradiation. *Journal of Nuclear Materials*, 340(2-3):187–202, Apr 2005.

102. R. J. Bruls, H. T. Hintzen, G. de With, and R. Metselaar. The temperature dependence of the Young's modulus of MgSiN₂, AlN and Si₃N₄. *Journal of the European Ceramic Society*, 21(3):263–268, Mar 2001.
103. Shoichi Kume, Masaki Yasuoka, Sang-Keel Lee, Akinori Kan, Hirota Ogawa, and Koji Watari. Dielectric and thermal properties of AlN ceramics. *Journal of the European Ceramic Society*, 27(8-9):2967–2971, 2007.
104. G. De With and N. Hattu. High-temperature fracture of hot-pressed AlN ceramics. *Journal of Materials Science*, 18(2):503–507, 1983.
105. Houssam A. Toutanji, David Friel, Tahar El-Korchi, R. Nathan Katz, Gary Wechsler, and William Rafaniello. Room temperature tensile and flexural strength of ceramics in AlN-SiC system. *Journal of the European Ceramic Society*, 15(5):425–434, 1995.
106. M. Fukuhara, A. Sanpei, and K. Shibuki. Low temperature-elastic moduli, Debye temperature and internal dilatational and shear frictions of fused quartz. *Journal of Materials Science*, 32(5):1207–1211, Mar 1997.
107. B. C. Daly, G. A. Antonelli, H. J. Maris, W. K. Ford, L. Wong, and E. Andideh. Measurements of the thermal conductivity of amorphous materials with low dielectric constants. *Physica B: Condensed Matter*, 316:254–257, May 2002.
108. R. Heidinger. Dielectric and mechanical properties of neutron irradiated KU1 and KS-4V glass. *Fusion Engineering and Design*, 66-68:843–848, 2003. 22nd Symposium on Fusion Technology.
109. J. Ye, N. Kojima, K. Furuya, F. Munakata, and A. Okada. Micro-thermal analysis of thermal conductance distribution in advanced silicon nitrides. *Journal of Thermal Analysis and Calorimetry*, 69(3):1031–1036, 2002.
110. K. Watari, K. Hirao, M. Toriyama, and K. Ishizaki. Effect of grain size on the thermal conductivity of Si₃N₄. *Journal of the American Ceramic Society*, 82(3):777–779, Mar 1999.
111. A. Kumar, T. Jayakumar, B. Raj, and K. K. Ray. Correlation between ultrasonic shear wave velocity and Poisson's ratio for isotropic solid materials. *Acta Materialia*, 51(8):2417–2426, May 2003.
112. DB Sirdeshmukh and KG Subhadra. Consistency checks on elastic properties of crystals. *Journal of Materials Science*, 40(7):1553–1570, Apr 2005.
113. E. A. Dean and J. A. Lopez. Empirical dependence of elastic-moduli on porosity for ceramic materials. *Journal of the American Ceramic Society*, 66(5):366–370, 1983.
114. KK PHANI and SK NIYOGI. Young modulus of porous brittle solids. *Journal of Materials Science*, 22(1):257–263, Jan 1987.
115. D. C. C. Lam, F. F. Lange, and A. G. Evans. Mechanical properties of partially dense alumina produced from powder compacts. *Journal of the American Ceramic Society*, 77(8):2113–2117, Aug 1994.
116. H. N. Yoshimura, A. L. Molisani, N. E. Narita, P. F. Cesar, and H. Goldenstein. Porosity dependence of elastic constants in aluminum nitride ceramics. *Materials Research*, 10(2):127–133, 2007.
117. D. P. H. Hasselman. On the porosity dependence of the elastic moduli of polycrystalline refractory materials. *Journal of the American Ceramic Society*, 45(9):452–453, 1962.
118. F. P. Knudsen. Dependence of mechanical strength of brittle polycrystalline specimens on porosity and grain size. *Journal of the American Ceramic Society*, 42(8):376–387, 1959.
119. R. Morrell. *Handbook of Properties of Technical & Engineering Ceramics: Part 1: An Introduction for the Engineer and Designer*. Her Majesty's Stationary Office, London, 1985.
120. S. P. Timoshenko and J. N. Goodier. *Theory of Elasticity*. Engineering Societies Monographs. McGraw-Hill Book Company, Singapore, 3rd edition, 1970.
121. AF Wright. Elastic properties of zinc-blende and wurtzite AlN, GaN, and InN. *Journal of Applied Physics*, 82(6):2833–2839, Sep 1997.
122. J. F. Nye. *Physical Properties of Crystals: Their Representation by Tensors and Matrices*. Clarendon Press, Oxford, 1957.
123. G. A. Alers and J. R. Neighbours. Crystal stability and elastic constants. *Journal of Applied Physics*, 28(12):1514–1514, 1957.
124. W. Voigt. *Lehrbuch der Kristallphysik (mit Ausschluss der Kristalloptik)*. B. G. Teubner, Leipzig, Germany, 1928.
125. A. Reuss. Berechnung der Fließgrenze von Mischkristallen auf Grund der Plastizitätsbedingung für Einkristalle. *Zeitschrift für Angewandte Mathematik und Mechanik / Journal of Applied Mathematics and Mechanics*, 9(1):49–58, 1929.
126. R. Hill. The elastic behaviour of a crystalline aggregate. *Proceedings of the Physical Society. Section A*, 65(5):349, 1952.
127. D. H. Chung and W. R. Buessem. The Voigt-Reuss-Hill approximation and elastic moduli of polycrystalline MgO, CaF₂, β -ZnS, ZnSe, and CdTe. *Journal of Applied Physics*, 38(6):2535–2540, 1967.
128. JB WACHTMAN, WE TEFFT, DG LAM, and CS APSTEIN. Exponential temperature dependence of Young's modulus of several oxides. *Physical Review*, 122(6):1754–1759, 1961.

129. R. G. Munro. Analytical representations of elastic moduli data with simultaneous dependence on temperature and porosity. *Journal of Research of the National Institute of Standards and Technology*, 109(5):497–503, Sep–Oct 2004.
130. O. L. Anderson. Derivation of wachtmans equation for temperature dependence of elastic moduli of oxide compounds. *Physical Review*, 144(2):553–557, 1966.
131. JB WACHTMAN and DG LAM. Young's modulus of various refractory materials as a function of temperature. *Journal of the American Ceramic Society*, 42(5):254–260, 1959.
132. M. Fukuhara and I. Yamauchi. Temperature dependence of the elastic moduli, dilational and shear internal frictions and acoustic-wave velocity for alumina, (Y)TZP and β' -sialon ceramics. *Journal of Materials Science*, 28(17):4681–4688, Sep 1993.
133. A Wolfenden. Measurement and analysis of elastic and anelastic properties of alumina and silicon carbide. *Journal of Materials Science*, 32(9):2275–2282, May 1997.
134. E. Sánchez-González, P. Miranda, J. J. Meléndez-Martínez, F. Guiberteau, and A. Pajares. Temperature dependence of mechanical properties of alumina up to the onset of creep. *Journal of the European Ceramic Society*, 27(11):3345 – 3349, 2007.
135. J. M. Staehler, W. W. Predebon, B. J. Pletka, and G. Subhash. Micromechanisms of deformation in high-purity hot-pressed alumina. *Materials Science and Engineering: A - Structural Materials: Properties, Microstructure and Processing*, 291(1-2):37 – 45, 2000.
136. CK UNNI and DE GORDON. Mechanical properties of monolithic AlN and SiC/AlN composites. *Journal of Materials Science*, 30(5):1173–1179, Mar 1995.
137. H. J. McSkimin. Measurement of elastic constants at low temperatures by means of ultrasonic waves - data for silicon and germanium single crystals, and for fused silica. *Journal of Applied Physics*, 24(8):988–997, 1953.
138. H. J. McSkimin. Measurement of ultrasonic wave velocities and elastic moduli for small solid specimens at high temperatures. *Journal of the Acoustical Society of America*, 31(3):287–295, 1959.
139. M. Fukuhara and A. Sampei. Effects on high-temperature-elastic properties on alpha-/beta-quartz phase transition of fused quartz. *Journal of Materials Science Letters*, 18(10):751–753, May 1999.
140. E. H. Carnevale, G. S. Larson, and L. C. Lynnworth. Ultrasonic measurement of elastic moduli at elevated temperatures using momentary contact. *Journal of the Acoustical Society of America*, 36(9):1678–1684, 1964.
141. A. A. Wereszczak, M. K. Ferber, M. G. Jenkins, C. K. J. Lin, K. Breder, and T. P. Kirkland. High-temperature mechanical performance of hot isostatically pressed silicon nitride. Technical Report ORNL/TM-12943, Oak Ridge National Laboratory, Oak Ridge, Tennessee, U.S.A., January 1996.
142. Qing Xia, Hui Xia, and Arthur L. Ruoff. Pressure-induced rocksalt phase of aluminum nitride: A metastable structure at ambient condition. *Journal of Applied Physics*, 73(12):8198–8200, 1993.
143. M UENO, A ONODERA, O SHIMOMURA, and K TAKEMURA. X-ray observation of the structural phase-transition of aluminum nitride under high-pressure. *Physical Review B*, 45(17):10123–10126, May 1992.
144. Feng Peng, Dong Chen, Hongzhi Fu, and Xinlu Cheng. The phase transition and the elastic and thermodynamic properties of AlN: First principles. *Physica B: Condensed Matter*, 403(23-24):4259–4263, 2008.
145. R. M. Hazen and L. W. Finger. High-pressure and high-temperature crystal chemistry of beryllium oxide. *Journal of Applied Physics*, 59(11):3728–3733, 1986.
146. C. F. Cline and D. R. Stephens. Volume compressibility of BeO and other II-VI compounds. *Journal of Applied Physics*, 36(9):2869–2873, 1965.
147. S. Spinner and W. E. Tefft. A method for determining mechanical resonance frequencies and for calculating elastic moduli from these frequencies. In *Proceedings, ASTM*, page 1221U1238, 1961.
148. M. E. Kipp and D. E. Grady. Shock phase transformation and release properties of aluminum nitride. *Journal de Physique IV*, 4(C8):249–256, Sep 1994.
149. C. F. Cline, H. L. Dunegan, and G. W. Henderson. Elastic constants of hexagonal BeO, ZnS, and CdSe. *Journal of Applied Physics*, 38(4):1944–1948, 1967.
150. RW Rice. Effects of environment and temperature on ceramic tensile strength grain size relations. *Journal of Materials Science*, 32(12):3071–3087, 1997.
151. J. Koike, S. Tashima, S. Wakiya, K. Maruyama, and H. Oikawa. Mechanical properties and microstructure of centrifugally compacted alumina and hot-isostatically-pressed alumina. *Materials Science and Engineering: A - Structural Materials: Properties, Microstructure and Processing*, 220(1-2):26 – 34, 1996.
152. GF RAISER, JL WISE, RJ CLIFTON, DE GRADY, and DE COX. Plate impact response of ceramics and glasses. *Journal of Applied Physics*, 75(8):3862–3869, Apr 1994.
153. H MIZUTA, K ODA, Y SHIBASAKI, M MAEDA, M MACHIDA, and K OHSHIMA. Preparation of high-strength and translucent alumina by hot isostatic pressing. *Journal of the American Ceramic Society*, 75(2):469–473, Feb 1992.

154. P. Boch, J. C. Glandus, J. Jarrige, J. P. Lecompte, and J. Mexmain. Sintering, oxidation and mechanical properties of hot pressed aluminium nitride. *Ceramics International*, 8(1):34 – 40, 1982.
155. J. C. Glandus, J. L. Besson, and P. Boch. High temperature properties of some nitrogen ceramics. *Science of Ceramics*, 11:419–424, 1981.
156. R Terao, J Tatami, T Meguro, and K Komeya. Fracture behavior of AlN ceramics with rare earth oxides. *Journal of the European Ceramic Society*, 22(7):1051 – 1059, 2002.
157. G. G. Bentle and R. M. Kniefel. Brittle and plastic behavior of hot-pressed BeO. *Journal of the American Ceramic Society*, 48(11):570–577, 1965.
158. MI Jones, H Hyuga, K Hirao, and Y Yamauchi. Highly transparent Lu-alpha-SiALON. *Journal of the American Ceramic Society*, 87(4):714–716, Apr 2004.
159. I. W. Chen and A. Rosenflanz. A tough SiAlON ceramic based on α -Si₃N₄ with a whisker-like microstructure. *Nature*, 389(6652):701–704, Oct 1997.
160. J Kim, A Rosenflanz, and IW Chen. Microstructure control of in-situ-toughened alpha-SiAlON ceramics. *Journal of the American Ceramic Society*, 83(7):1819–1821, Jul 2000.
161. C. Hazelton, J. Rice, L. L. Snead, and S. J. Zinkle. Effect of neutron radiation on the dielectric, mechanical and thermal properties of ceramics for rf transmission windows. *Journal of Nuclear Materials*, 253(1-3):190 – 195, 1998.
162. K. Hatanaka, H. Shiota, and T. Ando. Tensile test of sintered silicon nitride ceramic at elevated temperatures. *JSME (Japan Society of Mechanical Engineers) International Journal. Series 1, Solid Mechanics, Strength of Materials*, 34(3):351–360, 1991.
163. VJ Tennery, K Breder, MK Ferber, and MG Jenkins. Flexural fracture strength, fracture locations, and Monte Carlo predictions for a silicon nitride by ten US laboratories. *Journal of the American Ceramic Society*, 83(5):1177–1185, May 2000.
164. A. F. McLean and D. L. Hartsock. Design with structural ceramics. In J. B. Wachtman, editor, *Structural Ceramics: Treatise on Materials Science and Technology Volume 29*, pages 27–95. Academic Press, Inc., New York, 1989.
165. C. F. Robards and J. J. Gangler. Some properties of beryllium oxide and beryllium oxide - columbium ceramals. Technical Report NACA Research Memorandum E50G21, Lewis Flight Propulsion Laboratory, Cleveland, Ohio, U.S.A., March 2nd 1951.
166. VJ Tennery, K Breder, MK Ferber, and MG Jenkins. Tensile fracture behavior of two types of silicon nitride specimen geometries conducted by ten US groups. *Journal of the American Ceramic Society*, 83(5):1186–1191, May 2000.
167. G Subhash and G Ravichandran. Mechanical behaviour of a hot pressed aluminum nitride under uniaxial compression. *Journal of Materials Science*, 33(7):1933–1939, Apr 1998.
168. K. K. Kelley. High-temperature heat-content, heat-capacity, and entropy data for the elements and inorganic compounds. Technical report, United States Department of the Interior, Bureau of Mines, Washington, 1960.
169. O. A. Sergeev, A. G. Shashkov, and A. S. Umanskii. Thermophysical properties of quartz glass. *Journal of Engineering Physics and Thermophysics*, 43:1375–1383, 1982.
170. GK White and ML Mingos. Thermophysical properties of some key solids: An update. *International Journal of Thermophysics*, 18(5):1269–1327, Sep 1997.
171. D. Sedmidubský and J. Leitner. Calculation of the thermodynamic properties of a⁽ⁱⁱⁱ⁾ nitrides. *Journal of Crystal Growth*, 286(1):66–70, Jan 2006.
172. K. K. Kelley. The specific heats at low temperatures of beryllium oxide and beryllium orthosilicate (phenacite). *Journal of the American Chemical Society*, 61(5):1217–1218, 1939.
173. A. C. Victor and T. B. Douglas. Thermodynamic properties of magnesium oxide and beryllium oxide from 298 to 1,200 °K. *Journal of Research of the National Bureau of Standards A: Physics and Chemistry*, 67A(4):325–329, 1963.
174. H. Inaba. Semi-empirical estimation of constant-pressure heat capacities of binary oxides. *Journal of Phase Equilibria*, 20(3):187–192, Jun 1999.
175. R.W. Swindeman. Thermal shock tests on beryllia. *Journal of Nuclear Materials*, 14:404 – 415, 1964.
176. R. Berman. *Thermal Conduction in Solids*. Clarendon Press, Oxford, 1976.
177. R. J. Bruls, H. T. Hintzen, and R. Metselaar. A new estimation method for the intrinsic thermal conductivity of nonmetallic compounds: A case study for MgSiN₂, AlN and β -Si₃N₄ ceramics. *Journal of the European Ceramic Society*, 25(6):767 – 779, 2005.
178. K Hirao, K Watari, ME Brito, M Toriyama, and S Kanzaki. High thermal conductivity in silicon nitride with anisotropic microstructure. *Journal of the American Ceramic Society*, 79(9):2485–2488, Sep 1996.
179. J. R. Drabble and H. J. Goldsmid. *Thermal Conduction in Semiconductors*. International Series of Monographs on Semiconductors, Volume 4. Pergamon Press, Oxford, England, 1961.
180. R. J. Abraitis, A. K. Dargis, A. A. Rusyatskas, and E. J. Sakalauskas. A study of thermal conductivity of structural ceramic materials. part i. state of research of thermal conductivity of structural materials. *Refractories and Industrial Ceramics*, 40(7-8):351–358, Jul-Aug 1999.

181. W. D. Kingery, J. Francl, R. L. Coble, and T. Vasilos. Thermal conductivity. 10. Data for several pure oxide materials corrected to zero porosity. *Journal of the American Ceramic Society*, 37(2):107–110, 1954.
182. A. AlShaikhi and G. P. Srivastava. Thermal conductivity of single crystal and ceramic AlN. *Journal of Applied Physics*, 103(8):083554, Apr 2008.
183. A. Geith, M. Kulig, T. Hofmann, and C. Russel. Thermal conductivity of calcium-doped aluminum nitride ceramics. 1. Conventionally produced ceramics. *Journal of Materials Science*, 28(4):865–869, Feb 1993.
184. A. AlShaikhi and G. P. Srivastava. Drop and recovery of thermal conductivity of AlN upon UV irradiation. *Journal of Physics: Conference Series*, 92(1):012084, 2007.
185. J. H. Harris, R. C. Enck, and R. A. Youngman. Photoinduced thermal-conductivity changes in aluminum nitride. *Physical Review B*, 47(9):5428–5431, Mar 1993.
186. A. SUGAWARA. Precise determination of thermal conductivity of high purity fused quartz from 0 degrees to 650 degrees C. *Physica*, 41(3):515–520, 1969.
187. J. S. Haggerty and A. Lightfoot. Opportunities for enhancing the thermal conductivity of SiC and Si₃N₄ ceramics through improved processing. *Ceramic Engineering and Science Proceedings*, 16(4):475–487, 1995.
188. K. Watari, BC Li, L. Pottier, D. Fournier, and M. Toriyama. Thermal conductivity of beta-Si₃N₄ single crystal. In N. Murata, K. Shinozaki, and T. Kimura, editors, *Electroceramics in Japan III*, volume 181-1 of *Key Engineering Materials*, pages 239–242. Trans Tech Publications Ltd, 2000.
189. DT Morelli and JP Heremans. Thermal conductivity of germanium, silicon, and carbon nitrides. *Applied Physics Letters*, 81(27):5126–5128, Dec 2002.
190. N. Hirosaki, S. Ogata, C. Kocer, H. Kitagawa, and Y. Nakamura. Molecular dynamics calculation of the ideal thermal conductivity of single-crystal alpha- and beta-Si₃N₄. *Physical Review B*, 65(13):134110, Apr 2002.
191. Y. Akimune, F. Munakata, K. Matsuo, N. Hirosaki, Y. Okamoto, and K. Misono. Raman spectroscopic analysis of structural defects in hot isostatically pressed silicon nitride. *Journal of the Ceramic Society of Japan*, 107(4):339–342, 1999.
192. Koji WATARI, Yoshiyuki SEKI, and Kozo ISHIZAKI. Thermal properties of HIP sintered silicon nitride. *Journal of the Ceramic Society of Japan*, 97(1):56–62, 1989.
193. K. NEGITA. Effective sintering aids for Si₃N₄ ceramics. *Journal of Materials Science Letters*, 4(6):755–758, 1985.
194. N. Hirosaki, Y. Okamoto, M. Ando, F. Munakata, and Y. Akimune. Effect of grain growth on the thermal conductivity of silicon nitride. *Journal of the Ceramic Society of Japan*, 104(1):49–53, Jan 1996.
195. K. Watari, ME Brito, M. Toriyama, K. Ishizaki, S. Cao, and K. Mori. Thermal conductivity of Y₂O₃-doped Si₃N₄ ceramic at 4 to 1000 K. *Journal of Materials Science Letters*, 18(11):865–867, Jun 1999.
196. Bincheng Li, L. Pottier, J. P. Roger, D. Fournier, K. Watari, and K. Hirao. Measuring the anisotropic thermal diffusivity of silicon nitride grains by thermoreflectance microscopy. *Journal of the European Ceramic Society*, 19(8):1631 – 1639, 1999.
197. K. Watari, K. Hirao, ME Brito, M. Toriyama, and S. Kanzaki. Hot isostatic pressing to increase thermal conductivity of Si₃N₄ ceramics. *Journal of Materials Research*, 14(4):1538–1541, Apr 1999.
198. N. Hirosaki, Y. Okamoto, M. Ando, F. Munakata, and Y. Akimune. Thermal conductivity of gas-pressure-sintered silicon nitride. *Journal of the American Ceramic Society*, 79(11):2878–2882, Nov 1996.
199. Y. Okamoto, N. Hirosaki, M. Ando, F. Munakata, and Y. Akimune. Thermal conductivity of self-reinforced silicon nitride containing large grains aligned by extrusion pressing. *Journal of the Ceramic Society of Japan*, 105(7):631–633, Jul 1997.
200. K. Furuya, F. Munakata, K. Matsuo, Y. Akimune, J. Ye, and A. Okada. Microstructural control of beta-silicon nitride ceramics to improve thermal conductivity. *Journal of Thermal Analysis and Calorimetry*, 69(3):873–879, 2002.
201. Xinwen Zhu, You Zhou, Kiyoshi Hirao, and Zoltan Lencs. Processing and thermal conductivity of sintered reaction-bonded silicon nitride. I: Effect of Si powder characteristics. *Journal of the American Ceramic Society*, 89(11):3331–3339, Nov 2006.
202. Y. Okamoto, N. Hirosaki, M. Ando, F. Munakata, and Y. Akimune. Effect of sintering additive composition on the thermal conductivity of silicon nitride. *Journal of Materials Research*, 13(12):3473–3477, Dec 1998.
203. N. Hirosaki, M. Ando, Y. Okamoto, F. Munakata, Y. Akimune, K. Hirao, K. Watari, ME Brito, M. Toriyama, and S. Kanzaki. Effect of alignment of large grains on the thermal conductivity of self-reinforced beta-silicon nitride. *Journal of the Ceramic Society of Japan*, 104(12):1171–1173, Dec 1996.
204. Y. Akimune, F. Munakata, K. Matsuo, Y. Okamoto, N. Hirosaki, and C. Satoh. Effect of grain size and grain structure on the thermal conductivity of beta-si₃n₄. *Journal of the Ceramic Society of Japan*, 107(12):1180–1182, Dec 1999.

205. Naoto Hirosaki, Yusuke Okamoto, Fumio Munakata, and Yoshio Akimune. Effect of seeding on the thermal conductivity of self-reinforced silicon nitride. *Journal of the European Ceramic Society*, 19(12):2183 – 2187, 1999.
206. SK Lee, JD Moretti, MJ Readey, and BR Lawn. Thermal shock resistance of silicon nitrides using an indentation-quench test. *Journal of the American Ceramic Society*, 85(1):279–281, Jan 2002.
207. Hiroyuki Hayashi, Kiyoshi Hirao, Yukihiko Yamauchi, and Shuzo Kanzaki. Mechanical properties of high thermal conductivity silicon nitride. In *Annual Meeting of The Ceramic Society of Japan*, Tokyo, March 24 2003.
208. I. M. Abdulagatov, S. N. Emirov, T. A. Tsomaeva, K. A. Gairbekov, S. Y. Askerov, and N. A. Magomedova. Thermal conductivity of fused quartz and quartz ceramic at high temperatures and high pressures. *Journal of Physics and Chemistry of Solids*, 61(5):779–787, May 2000.
209. In-Sub Han, Doo-Won Seo, Sei-Young Kim, Ki-Seog Hong, Kil Ho Guahk, and Kee Sung Lee. Properties of silicon nitride for aluminum melts prepared by nitrated pressureless sintering. *Journal of the European Ceramic Society*, 28(5):1057 – 1063, 2008.
210. H Iwanaga, A Kunishige, and S Takeuchi. Anisotropic thermal expansion in wurtzite-type crystals. *Journal of Materials Science*, 35(10):2451–2454, May 2000.
211. Glen A. Slack and S. F. Bartram. Thermal expansion of some diamondlike crystals. *Journal of Applied Physics*, 46(1):89–98, 1975.
212. D.G. Walker, R.M. Mayer, and B.S. Hickman. X-ray diffraction studies of irradiated beryllium oxide. *Journal of Nuclear Materials*, 14:147 – 158, 1964.